Delft University of Technology

Topology optimization to eliminate cavities and internal supports in AM-produced formwork for functional structure fabrication

Tong, Wei; Wu, Jun; Weng, Yiwei

Topology optimization to eliminate cavities and internal supports in AM-produced formwork for functional structure fabrication

Wei Tong[1] · Jun Wu[2] · Yiwei Weng[1] 🄳

Abstract

Additive manufacturing (AM) facilitates the production of complex structures. It is often combined with structural design by topology optimization to create lightweight structures with minimal material and maximum stiffness. In this paper, we consider the design of lightweight structures to be created by casting in formwork that is produced by additive manufacturing. This problem, arising from the building industry, relates to but differs from prior work on topology optimization for structures that are directly produced by additive manufacturing. Specifically, formwork is not permitted to contain extra supports in casting space since otherwise it results in casting blockages. Moreover, topological structures with cavities cannot be produced through casting. This work presents a topology optimization method for designing structures to be cast in AM-produced formwork. This approach addresses these two key challenges: (i) ensuring the formwork is self-supporting during printing to eliminate the need for additional supports, and (ii) designing the structure to be free of internal enclosed cavities, which would otherwise lead to disconnected or floating parts in the formwork. The effectiveness of the proposed method was demonstrated through several numerical examples and experimental evaluations. Results show that the formwork can be printed without extra supports, and internal enclosed cavities in optimized structures can be fully eliminated. The findings provide a new strategy to produce the lightweight structure and corresponding structural formwork.

Keywords Formwork · Self-supporting design · Connectivity · Topology optimization · Additive manufacturing

1 Introduction

Formwork plays an important role in shaping the casting materials into the desired geometry in the building industry. It can be used to produce high-performance and material-efficient lightweight structures. Additive manufacturing (AM) facilitates the production of formwork for complex lightweight structures. In the manufacturing process, there are two key requirements: (i) support-free printability during printing and (ii) castability of the lightweight structures during casting. It is essential to consider the design requirements to facilitate manufacturing and promote practical application.

AM is a set of technologies that creates 3D objects by adding material layer by layer. It offers advantages such as high material efficiency, design flexibility, and adaptability (Abdulhameed et al. 2019; Gibson et al. 2021; Wong and Hernandez 2012). AM has attracted significant interests across a diverse array of industrial applications, including aerospace (Najmon et al. 2019), building construction (Weng et al. 2020), and biomedical fields (Singh and Ramakrishna 2017). In particular, fused filament fabrication (FFF) is the most widely used due to its cost-effectiveness and operational simplicity (Kristiawan et al. 2021). FFF has been applied in formwork production in the building industry to construct complex functional structures (Jipa and Dillenburger 2022). Compared to other fabrication methods, such as 3D concrete printing (3DCP) (Bos et al. 2016), structures to be fabricated by casting in AM-produced formwork can mitigate cold-joint effects due to the layer-wise process (Ma et al. 2019). Leschok and Dillenburger (2019) introduced a water-dissolvable 3D printed formwork to facilitate

✉ Yiwei Weng
   yiwei.weng@polyu.edu.hk

1 Department of Building and Real Estate, The Hong Kong Polytechnic University, Hong Kong 999077, China

2 Department of Sustainable Design Engineering, Delft University of Technology, 2628 CE Delft, The Netherlands

formwork removal. Burger et al. (2020) proposed a system for collaborative manufacturing of ultra-thin formwork and casting process. Jipa et al. (2020) investigated the fabrication of submillimetre-thin formwork for producing geometrically complex concrete parts. The above-mentioned studies fabricated column structures with complex shapes and inclination angles for architectural purposes without taking mechanical performance into account.

The primary advantage of AM is its capacity to fabricate complex structures and geometries, thereby rendering complex designs viable, such as topology-optimized lightweight structures. Topology optimization is a mathematical method by determining the most efficient material distribution within a specified design space to enhance mechanical performance (Sigmund and Maute 2013). It has experienced substantial developments, driven by the introduction of various influential methods, including the Solid Isotropic Microstructure with Penalization (SIMP) method (Bendsoe and Sigmund 2013; Sigmund 2001), (Bi-directional) Evolutionary Structural Optimization (ESO) method (Huang and Xie 2007, 2010; Xie and Steven 1992, 1993), level set method (Allaire et al. 2002; Sethian and Wiegmann 2000; Wang et al. 2003), Moving Morphable Components (MMC) (Guo et al. 2014; Zhang et al. 2016) and Voids (MMV) (Zhang et al. 2017, 2018). Structures generated by topology optimization frequently exhibit intricate geometries that are challenging to realize using conventional manufacturing methods.

Notwithstanding the significant synergy between topology optimization and FFF, many challenges persist in practical implementations of fabricating complex formwork by FFF in the building industry, including anisotropic behavior (Li et al. 2020, 2022), overhang angle (Bi et al. 2020; Langelaar 2016), and connectivity (Xiong et al. 2020; Zhou and Zhang 2019). In this paper, it is crucial to address challenges related to connectivity and overhang issues within a printed structure by employing FFF to fabricate formwork for topological structures. The connectivity of the component is an intuitive issue, as structures with internal enclosed cavities cannot be produced using formwork, as shown in Fig. 1. Furthermore, the infeasible overhanging surfaces are another widely recognized issue in 3D printing. The formwork is a hollow structure that serves as a casting container, and

therefore, to ensure casting quality and flowability, the casting space must be completely hollow without any additional printed support materials, as shown in Fig. 2.

Existing studies have addressed the connectivity and overhang problems of topology-optimized structures rather than the corresponding formwork. For the connectivity issue, Zhou and Zhang (2019) employed closed B-splines and super-ellipses to control enclosed cavities in optimized structures. Zhao et al. (2020) proposed a direct approach to controlling the connectivity of the optimized structures. Xiong et al. (2020) eliminate enclosed cavities based on the graph theory and BESO framework. These studies address the connectivity of optimized structures. However, the overhang issue induced by the 3D printing process still cannot be solved simultaneously. For the overhang issue, much research has been done to optimize structures directly to enable self-supporting printing within the established three-axis printing system. Brackett et al. (2011) proposed quantifying the angle of the overhanging part of a 2D design as a penalty function for optimizing the structure. Gaynor et al. (2014) introduced a wedge-shaped filter to represent the support conditions. Qian (2017) employed a projection-based technique to prevent the generation of overhanging features. Langelaar proposed both 2D (2017) and 3D (2016) filters tailored for AM, aimed at generating self-supporting features in alignment with AM processes. Guo et al. (2017) applied the explicit MMC and MMV frameworks to establish the self-supporting structure. Bi et al. (2020) introduced a geometric self-supporting constraint within the topology optimization framework of BESO. In summary, these efforts aim to enable direct support-free printing of topology-optimized components. However, the capability to print topology-optimized components directly does not necessarily imply that the corresponding formwork can be fabricated in an internally unsupported manner, as shown in Fig. 3.

This work aims to develop an innovative topology optimization method compatible with density-based topology optimization approaches, addressing the connectivity issues of topology-optimized structures and enabling support-free printing of the corresponding formwork. The proposed methodology prioritizes the mechanical properties of the
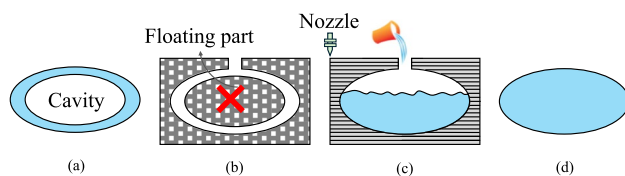
Fig. 1 **a** Target structure with internal enclosed cavity; **b** Corresponding formwork with internal floating part, unmanufacturable by FFF; **c** Manufacturable formwork part by FFF; **d** Actual casting structure without internal enclosed cavity using AM-produced formwork
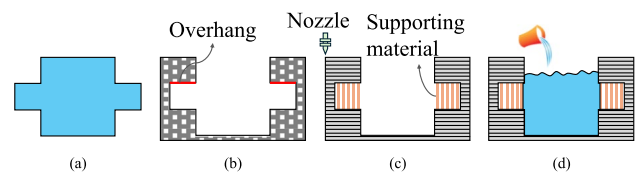
Fig. 2 **a** Objective structure; **b** Schematic figure of corresponding formwork with overhanging surfaces; **c** Printed formwork incorporates the orange internal support material under infeasible overhanging surfaces; **d** Illustration of blockage of casting due to internal support material

Fig. 3 Illustration of the overhanging feature of objective structure and corresponding formwork for 3D printing: **a** Objective structure without overhanging surfaces; **b** Corresponding formwork with overhanging surfaces

structure as the primary optimization objective. While minimizing structural compliance, this method ensures both the connectivity of the structure and the internal support-free printability of th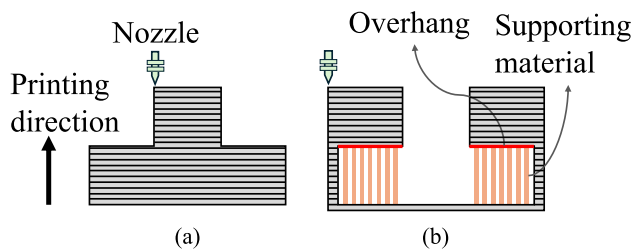e corresponding formwork. This method is significant for the printing of casting formwork, which can be manufactured without the need for sacrificial supports. It reduces the difficulty of the manufacturing process and manufacturing costs.

The paper is organized as follows: Sect. 2 provides a detailed explanation of the self-supporting method and the formulation of the topology optimization problem. Section 3 presents four numerical examples. Section 4 proposes an extension strategy of the framework to diverse overhang angles. Section 5 demonstrates the 3D printed formwork, cast samples, and strength tests. The conclusion is presented in Sect. 6.

2 Computational method

2.1 Overhang angle definition

In AM, a self-supporting structure is characterized by its ability to be fabricated without needing supplementary support materials and maintaining stability throughout the printing process. This indicates that the material of each successive layer can be deposited on the preceding layer without experiencing collapse. The overhang angle serves as the critical determinant for self-supporting capability, which can be defined in relation to the outward-facing normal vector (**n**) and the printing direction. As illustrated in Fig. 4, the overhang angle (α) is defined as the angle between the structural surface and the baseplate, which can be mathematically represented as follows:

$$\alpha = \pi - \theta \tag{1}$$

where θ is the angle between the normal vector and the printing direction. When α exceeds the threshold beyond which the 3D printer can effectively print, the material deposition is deemed unsuccessful.

The threshold for the overhang angle is affected by various factors, including printer specifications, the type of print material, and the specific printing technology employed. A typical value of 45° has been adopted and validated in several studies as effective for achieving self-support and ensuring surface print quality (Kranz et al. 2015; Mertens et al. 2014; Wang et al. 2013).

2.2 Numerical representation of AM formwork filter

In topology optimization, the self-supporting characteristic is illustrated using geometric terminology. To facilitate expression and elucidate the relationship between self-supporting structures and mathematical geometry, the

Fig. 4 **a** Graphic presentation of 3D printed structure with the overhang portion highlighted in blue; **b** Feasible structure for printing under a 45° overhang angle constraint
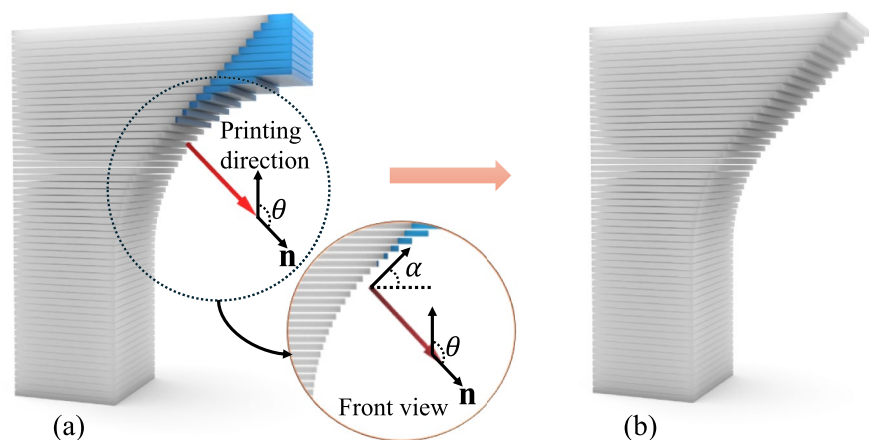
design domain is discretized into uniform cuboid elements with the size of $l_x \times l_y \times l_z$ using the finite element method (Fig. 5b). Constraints for various overhang angles can be imposed by adjusting the dimensions of the cuboid elements. In Sect. 3, a typical overhang constraint value of 45° is employed, whereby the entire design domain is discretized into $n_x \times n_y \times n_z$ cubic elements (with $l_x = l_y = l_z$) along the three coordinate axes. To enhance the applicability of the approach across diverse AM technologies, an extension method of variable overhang angles is provided in Sect. 4.

In the SIMP framework, density variables denote the relative amount of material within each element and are constrained within the range of 0 (void) to 1 (solid), which can be donated as $0 \le x_{(i,j,k)} \le 1$. In this notation, the footnote indices i, j, and k indicate the element's position in the x, y, and z directions, respectively. Consequently, the printed baseplate has $j = 1$ in the y-direction. The conventional SIMP approach primarily focuses on structural performance but does not inherently address the issue of structural overhang. In AM process, the underlying layer can provide structural support for the subsequent layers. The AM formwork filter is inspired by the layer-by-layer deposition process in additive manufacturing. In this approach, the actual printing elements $p_{(i,j,k)}$ are defined in terms of the blueprint density $x_{(i,j,k)}$ and bottom supporting density $b_{(i,j,k)}$. As depicted in Fig. 5c, the condition required for the upper green element to be adequately supported is contingent upon the densities of the five neighboring lower black elements. If at least one of the five lower elements is solid, the element (i,j,k) is deemed supportable. Likewise, a solid element (i,j,k) possesses the capability to support the five neighboring elements above it.

The above-mentioned self-supporting method is straightforward to implement for binary elements with densities of 0 or 1. Due to the intermediate density characteristic inherent in the SIMP method, defining the density of the actual printed element $p_{(i,j,k)}$ cannot be higher than printable density $p_{a(i,j,k)}$. The printable density p_a is determined by the maximum density

among the five lower neighboring elements $b_{(i,j,k)}$. Therefore, the modified self-supporting method can be formulated as follows:

$$p_{(i,j,k)} = \min \left(x_{(i,j,k)}, p_{a(i,j,k)} \right) \tag{2}$$

$$p_{a(i,j,k)} = \max \left(p \in b_{(i,j,k)} \right) \tag{3}$$

Considering the max and min functions are not differentiable, a smooth strategy is employed to overcome this difficulty:

$$\min \left(x, p_a \right) = p \approx \frac{1}{2} \left(x + p_a - \sqrt{(x - p_a)^2 + \varepsilon} + \sqrt{\varepsilon} \right) \tag{4}$$

$$\max \left(p \in b \right) = p_a \approx \frac{\sum\limits_{e \in b} p_e \exp \left(\alpha p_e \right)}{\sum\limits_{e \in b} \exp \left(\alpha p_e \right)} \tag{5}$$

where ε and α are artificially defined parameters used to regulate the smoothness and approximate accuracy. As ε approaches 0 and α approaches ∞, p and p_a converge to $\min(x, p_a)$ and $\max(p \in b)$, respectively. A smaller value of ε or a larger value of α will increase the nonlinearity and ill-conditioning of the problem. In this case, the following specific values are chosen:

$$\varepsilon = 10^{-4}, \alpha = 30 \tag{6}$$

Rewriting Eqs. (4 and 5) in vector form, we have

$$\mathbf{p}_j = \frac{1}{2} \left(\mathbf{x}_j + \mathbf{p}_{a,j} - \left[(\mathbf{x}_j - \mathbf{p}_{a,j})^{\circ 2} + \varepsilon \right]^{\circ 1/2} + \sqrt{\varepsilon} \right) \tag{7}$$

$$\mathbf{p}_{a,j} = \left\{ \mathbf{H}_b \left[\mathbf{p}_{j-1} \circ \exp \left(\alpha \mathbf{p}_{j-1} \right) \right] \right\} ./ \left[\mathbf{H}_b \exp \left(\alpha \mathbf{p}_{j-1} \right) \right] \tag{8}$$

where $\mathbf{p}$, $\mathbf{x}$, $\mathbf{p}_a$ are density field vectors, the subscript j is the layer index, "$\circ$" represents Hadamard product (i.e.,

Fig. 5 **a** Graphical representation of the stacking of 3D printing filament layers; **b** Geometric representation of finite element discretization of printing filaments; **c** Geometric definition of the self-supporting method for the 3D AM formwork filter
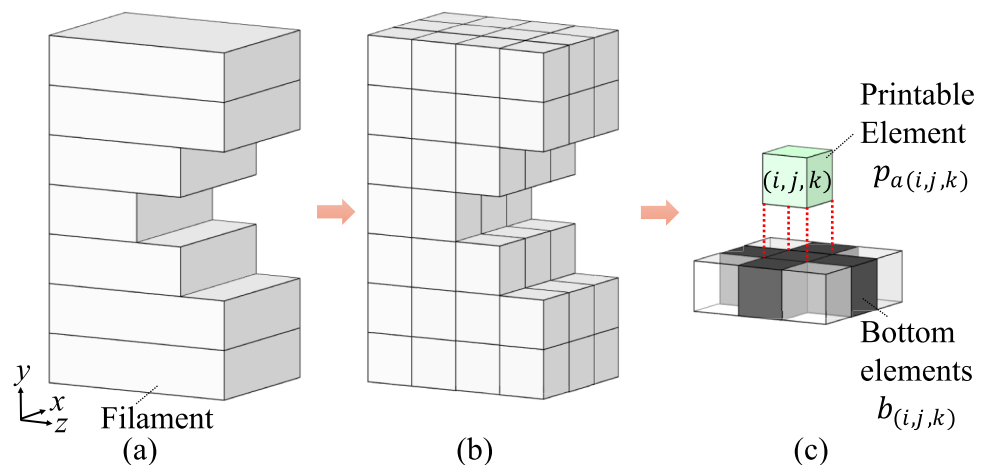
element-wise product), and "./" denotes element-wise division, the matrix $\mathbf{H}_b$ is the convolution operator containing information of underlying elements b. For $e \in b$, as given in Eq. (5), the value in $\mathbf{H}_b$ is $H_b = 1$, otherwise, $H_b = 0$. It should be noted that other smooth strategies are acceptable. The principle of selection is to ensure that the function is smooth and differentiable to facilitate gradient-based updating. Equations. (7 and 8) yield good behavior in this work.

A preliminary test has been performed to assess the effectiveness of the proposed AM formwork filter. Figure 6
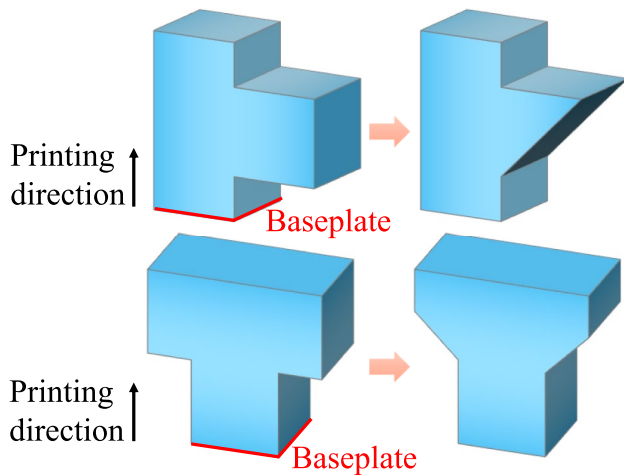

Fig. 6 Effectiveness tests of the AM formwork filter with 45° overhang constraint: original density field (left) and filtered density field (right)

illustrates the structure after applying the proposed AM formwork filter with a 45° overhang constraint. After filtering, overhang parts are removed, retaining only the components that comply with the printing constraints.

It is crucial to highlight that the proposed AM formwork filter effectively resolves both the self-supporting issue of the formwork and the connectivity issue of the objective structures simultaneously. As illustrated in Fig. 1, the internal enclosed cavities in the objective structures correspond to floating parts in the formwork. Therefore, addressing the self-supporting issue of the formwork consequently eliminates these floating parts, thereby ensuring the absence of internal enclosed cavities within the objective structures.

2.3 Topology optimization for self-supporting formwork

Figure 7 illustrates a conceptual optimization process. The design domain and boundary conditions are initialized before optimization, as depicted in Fig. 7a. A structural density field $\mathbf{x}$ (Fig. 7b) can be obtained after successive iterations of the optimization process under the specified constraints and boundary conditions. It is important to note that the objective is to achieve self-supporting 3D printing for formwork. Therefore, it is essential to derive the corresponding formwork density field from the obtained topological structure. To ensure self-supporting behavior at the periphery and bottom of the formwork, Dirichlet boundaries are implemented with an extension of one discrete element thickness around the design
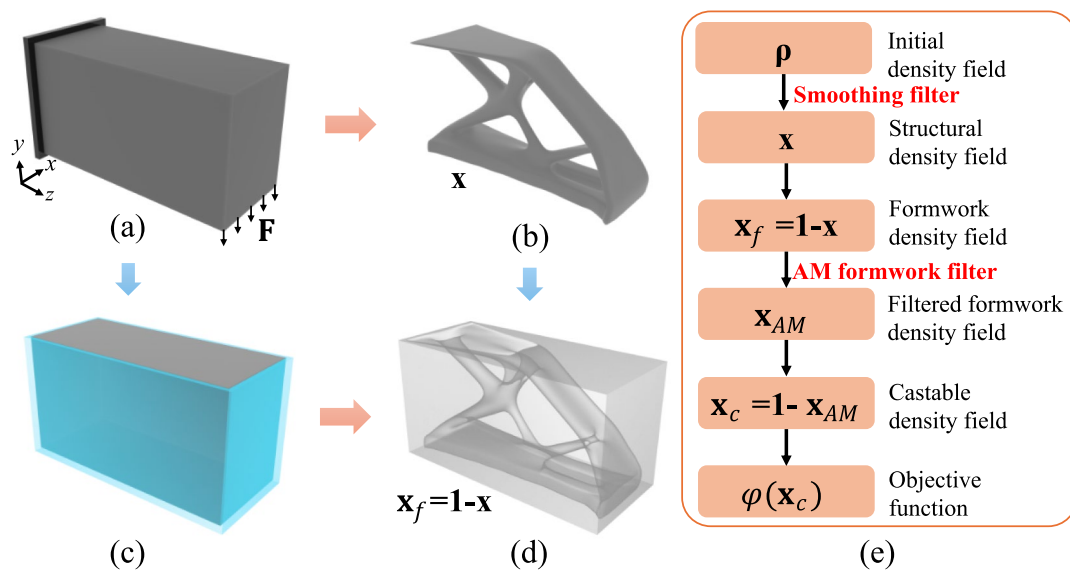

Fig. 7 Graphic illustration of topology optimization with AM formwork: **a** Design domain and boundary conditions; **b** Topology-optimized structure; **c** Extended Dirichlet boundaries (blue) around design domain for formwork design; **d** Castable formwork; **e** Five-field density filtering strategy for castable formwork optimization

domain, maintaining a constant formwork density of 1. Figure 7c highlights the Dirichlet boundaries with blue-colored parts. Consequently, the formwork density field $\mathbf{x}_f$ (Fig. 7d) can be represented as follows:

$$\mathbf{x}_f = 1 - \mathbf{x} \qquad (9)$$

Figure 7e illustrates the density field filtering strategy employed for optimizing castable formwork. The AM formwork filter proposed in Sect. 2.2 is adopted to perform filtering operations on the formwork density field $\mathbf{x}_f$ to obtain the filtered formwork density $\mathbf{x}_{AM}$. This filtering operation aims to preserve self-supporting materials, while eliminating non-self-supporting materials from the formwork. Similarly, the density field of a corresponding castable topology $\mathbf{x}_c$ can be derived from the filtered formwork density $\mathbf{x}_{AM}$, and it can be expressed as follows:

$$\mathbf{x}_c = 1 - \mathbf{x}_{AM} \qquad (10)$$

In addition to the AM formwork filter, a smoothing filter is employed to eliminate checkerboard patterns in topology optimization, thereby preventing the formation of regions with alternating black and white elements (Andreassen et al. 2011; Sigmund 2007). The smooth filtering operation is applied before the structural density field $\mathbf{x}$ to ensure that the resulting structure exhibits a good topological configuration. Therefore, the structure density field $\mathbf{x}$ is explicitly defined as follows:

$$\mathbf{x} = \mathbf{H}_s \boldsymbol{\rho} \qquad (11)$$

where $\boldsymbol{\rho}$ is the initial design density vector, $\mathbf{H}_s$ is the weighted convolution matrix for smooth filtering. The entry in the e-th row and i-th column of $\mathbf{H}_s$ matrix is determined as follows:

$$\left(\mathbf{H}_s\right)_{e,i} = \frac{H_{ei}}{\sum_{i \in N_e} H_{ei}} \qquad (12)$$

where N_e is the set of element i within a ball, where its centroid-to-centroid distance to element e is less than the radius r_{min} (i.e., $\Delta(e,i) < r_{min}$), H_{ei} is the convolution operator, which is expressed in terms of $\Delta(e,i)$:

$$H_{ei} = \max(0, r_{min} - \Delta(e,i)) \qquad (13)$$

Therefore, the density field progresses through five evolutionary stages of $\boldsymbol{\rho} \rightarrow \mathbf{x} \rightarrow \mathbf{x}_f \rightarrow \mathbf{x}_{AM} \rightarrow \mathbf{x}_c$, and this sequence is referred to as the five-field density approach. The application of density filters results in the initial density vector $\boldsymbol{\rho}$ losing its physical significance. Therefore, the optimization function φ is defined in terms of the final castable density field $\mathbf{x}_c$.

2.4 Optimization problem formulation

The compliance minimization problem is a fundamental problem in topology optimization, aiming to optimize structural designs to reduce strain energy under external loads. The optimization problem is formulated as follows:

$$\begin{aligned} \min_{\mathbf{x}_c} &: c(\mathbf{x}_c) = \mathbf{F}^T \mathbf{U} \\ \text{Subject to} &: V(\mathbf{x}_c) = fV_0 \\ &\quad \mathbf{K}\mathbf{U} = \mathbf{F} \\ &\quad \mathbf{0} \le \mathbf{x}_c \le \mathbf{1} \end{aligned} \qquad (14)$$

where c is the compliance, $\mathbf{x}_c$ is the castable density field, $\mathbf{F}$ and $\mathbf{U}$ are the global node force vector and displacement vector, $V(\mathbf{x}_c)$ and V_0 denote the material volume and design domain volume, respectively, and f is the prescribed volume fraction of the design domain. $\mathbf{K}$ is the global stiffness matrix assembled from the element stiffness matrix $\mathbf{k}_e$, which is defined as follows:

$$\mathbf{k}_e = E_e(x_{c,e})\mathbf{k}_0, \ (x_{c,e} \in \mathbf{x}_c) \qquad (15)$$

where $\mathbf{k}_0$ is the element stiffness matrix with unit Young's modulus, E_e is the element stiffness interpolated by the solid (E_0) and void (E_{min}) stiffness, which is $E_e = E_{min} + (x_{c,e})^p(E_0 - E_{min})$. p is a penalization power factor introduced to drive the density field toward binary values of 0 and 1.

The sensitivities of the objective and constraints function are necessary to solve the optimization problem defined by Eq. (14) using the gradient information and Method of Moving Asymptotes (MMA) solver. The detailed sensitivity analysis is provided in Appendix A and B.

3 Numerical studies

This section presents the 3D numerical examples to demonstrate the effectiveness of the proposed five-field density approach and AM formwork filter. The entire design domain is discretized into hexahedral elements, with the density of each element updated utilizing the MMA solver. A sufficient number of convergence steps are employed to ensure that the structure attains a stable topology. The convergence criterion is stipulated as the relative change in compliance value between iteration step i and step i-4 is less than 0.1%. As the density field is discretized into hexahedral elements, a threshold value of 0.5 is utilized to extract the isosurface of the density field through triangle mesh representation for visualizing the 3D structure. Subsequently, quad-remeshing is employed to smooth the structure surface on the Rhinoceros platform, and overhang features are identified based on the post-processed structures.

Figure 8 illustrates the visualization and post-processing procedures. The Young's modulus and Poisson's ratio for the solid material are defined as 200 GPa and 0.3, respectively. To prevent checkerboard patterns, a smoothing filter radius defined in Eq. (13) is set to 3 for all cases. For the finite element analysis, the 8-node hexahedral elements with trilinear shape functions are utilized to compute node displacements. All optimizations and calculations are performed using MATLAB R2024a.

3.1 3D cantilever beam

Figure 9 shows the first example, which is a cantilever beam discretized by 8-node cubic elements with a resolution of $96 \times 48 \times 48$ to fit the structural design domain. All displacements at the plane of $z = 0$ are suppressed, and a total load of 100N is uniformly distributed on the lower edge of $z = z_{max}$ plane. A total volume fraction of 50% is employed as the constraint within the design domain.

Figure 10a presents the beam optimized without applying the AM formwork filter under the above parameter settings, whose compliance value is 74.61. It can be observed that the structure optimized using the classical approach exhibits internal enclosed cavities (Fig. 10b) that are unfeasible for manufacturing via formwork casting. Furthermore, the corresponding original formwork (Fig. 10c) is difficult to print using a three-axis FFF system due to pronounced geometric overhangs.

To quantify the printability of the formwork, two parameters are established: the infeasible overhanging surface fraction (f_{ios}) is defined as the ratio of the overhanging surface area to the internal cast surface area, and the internal enclosed cavities fraction (f_c) as the ratio of the volume of internal enclosed cavities to the total volume of design domain. The internal enclosed cavities fraction of the beam is $f_c = 7.5\%$. As depicted in Fig. 10d, the formwork surfaces with overhang angles greater than 45° are highlighted in red, and the infeasible overhanging surface fraction is $f_{ios} = 21.5\%$. The formwork depicted in
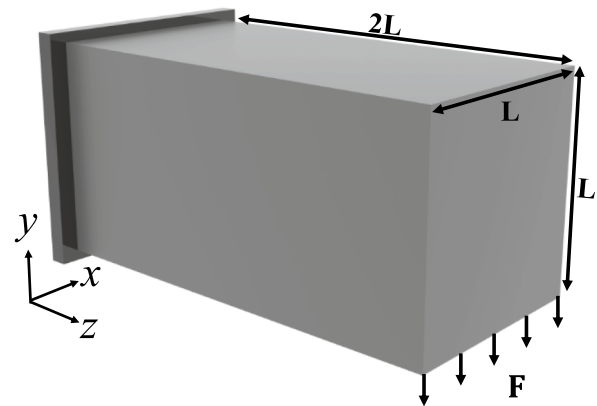
Fig. 9 Design domain and boundary conditions for cantilever beam problem in compliance minimization design

Fig. 10d exhibits significant manufacturing limitations that necessitate geometric post-processing to ensure producibility, including changing the overhanging surfaces and eliminating floating parts. Figure 10e illustrates the post-processed formwork following the application of the AM formwork filter, with the assumed printing direction from y_{min} to y_{max}, and the final castable cantilever beam is shown in Fig. 10f. It is evident that the geometry has undergone significant changes, the suspended cavity structures in the formwork have been eliminated, and both the top and bottom now exhibit a 45° beveled shape. It is important to emphasize that unprintable parts in the original formwork during post-processing are eliminated causing the structure to deviate from the initial design, ultimately resulting in the inability to preserve volume fraction. An increase in the volume fraction of the cast beam structure is observed, rising from the original 50% to 61.7%. Therefore, it is preferable to incorporate manufacturing constraints into the topology optimization process rather than using a post-processing approach to design a structure.
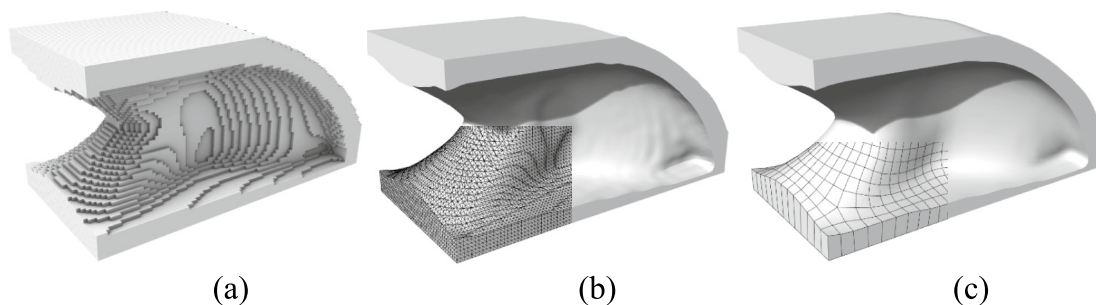
Fig. 8 Visualization and post-processing of the 3D structure: **a** Finite element discretization result; **b** Triangular mesh isosurface extracted using a density threshold of 0.5; **c** Smoothing post-processing through quad-remeshing

Fig. 10 **a** Topology-optimized cantilever beam by conventional method; **b** Illustration of internal enclosed cavities within the optimized cantilever beam; **c** Required formwork for constructing beam-(**a**); **d** The infeasible overhanging surfaces in formwork-(**c**) highlighted in red; **e** Manufacturable part of the formwork by FFF under 45° overhang constraint; **f** Castable cantilever beam from formwork-(**e**)


(a)

(b)

(c)

(d)

(e)

(f)
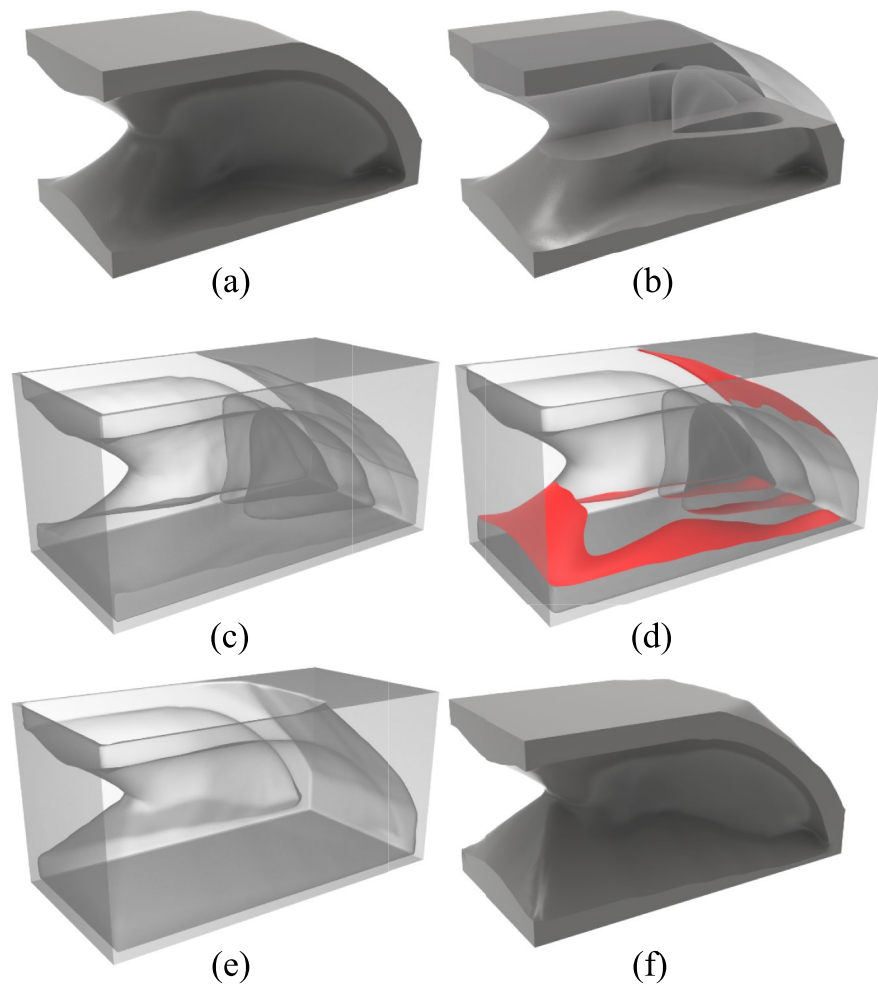
It is important to emphasize that the printable volume fraction of the formwork is dependent on the printing direction. The data presented above are quantified by printing with y_{min} as the baseplate. Given the presence of internal enclosed cavities within the original formwork, it is evident that complete fabrication of the formwork is unattainable regardless of the selected printing direction. Analogously, in the topology optimization process, results obtained by considering different formwork printing directions are expected to vary, which will be discussed in the subsequent paragraphs.

By incorporating the five-field density approach and the AM formwork filter into the topology optimization process, most infeasible overhanging features can be effectively mitigated. The occurrence of minor infeasible overhanging surfaces is due to post-processing, which is explained in detail in the later paragraphs. In this example, the cantilever beams are optimized using four distinct formwork printing directions, including defining y_{min}, y_{max}, z_{min}, and z_{max} as the baseplate for 3D printing, respectively. To account for the symmetry of the boundary conditions and the structure, and to avoid the creation of unnecessary lateral support

structures (Langelaar 2016), x_{min} and x_{max} are not chosen as the printed baseplate for optimization. The optimization results of cantilever beams for various formwork printing directions are illustrated in Fig. 11. Due to the impact of different printing directions on the geometric relationships of layer-by-layer supports during AM, the optimized designs are evidently influenced by the selected printing direction. The AM formwork filter algorithm adjusts the density field according to specific printing requirements, resulting in a design that is internally self-supporting for the formwork structure.

To evaluate the performance of the beams, a quantitative comparison of compliance value and normalized compliance percentages has been conducted and summarized in Table 1. Compared to the benchmark beam design (see Fig. 10a), the compliance of the results optimized using the five-field density approach increased by 121.8% to 167.0%. When y_{min} is defined as the baseplate for formwork printing, the compliance value increases the most, reaching 167.0%. Conversely, when z_{min} is used as the baseplate, the compliance increase is the lowest at 121.8%. The compliance for y_{max} is reported as 144.4%, while for z_{max} it is 129.4%.
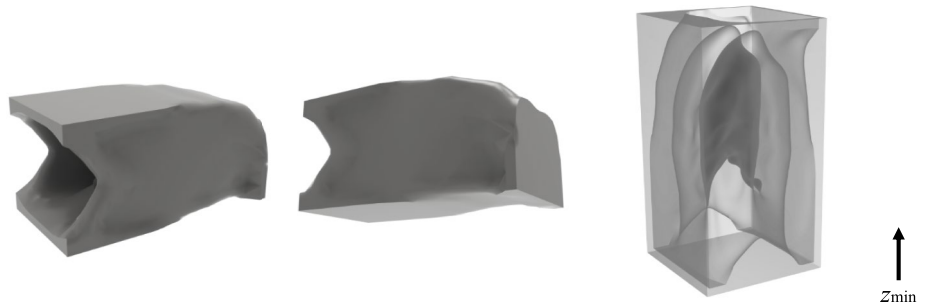
Fig. 11 Results of topology-optimized cantilever beams from different viewpoints (left & middle) and corresponding formwork (right) for various printing directions by five-field density approach
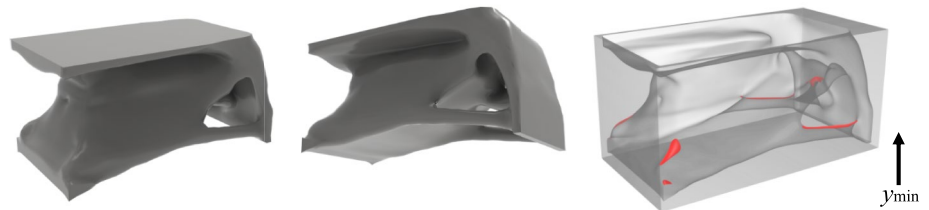
(a) Optimized beam with formwork printing direction of y_{min}
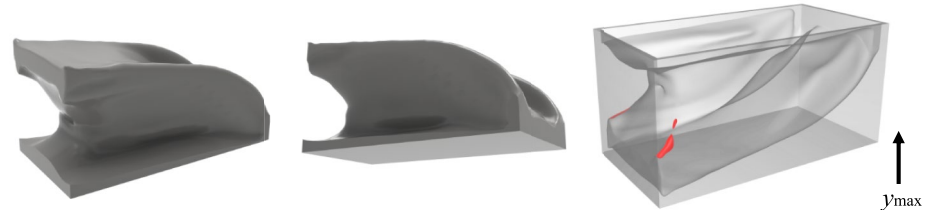
(b) Optimized beam with formwork printing direction of y_{max}

(c) Optimized beam with formwork printing direction of z_{min}

(d) Optimized beam with formwork printing direction of z_{max}

Table 1 A comparison analysis of cantilever beam results

Printing baseplate	f_{ios} (Formwork)	f_c (Beam)	Compliance (Beam)	Normalized compliance
Benchmark	21.5%	7.5%	74.61	100%
y_{min}	1.1%	0%	124.61	167.0%
y_{max}	0.4%	0%	107.74	144.4%
z_{min}	0%	0%	90.88	121.8%
z_{max}	0%	0%	96.54	129.4%

The observed increase in compliance is primarily attributed to the additional constraints, which cause the structure to deviate from the initially compliance-optimized design. This phenomenon is common in multi-constraint topology optimization. Additionally, due to the additional constraints, the structure often converges to local optima, complicating the search for a global optimum design under multiple constraints. This issue is prevalent in current optimization algorithms, and the impact of optimization setup parameters on the design results is beyond the scope of this study.

In addition, Table 1 presents the infeasible overhanging surface fraction (f_{ios}) of different formwork and the internal enclosed cavities fraction (f_c) of the cantilever

beams. Furthermore, Fig. 11 (right) visually highlights the internal surfaces of the formwork that do not satisfy the 45° overhang constraints in red. These results demonstrate that the proposed optimization method achieves 100% structural connectivity and effectively eliminates internal enclosed cavities. The f_{ios} value for formwork optimized with z_{min} and z_{max} as the printing baseplates is 0%, indicating that the formwork permits 100% internal unsupported printing. For the cases of printing baseplates of y_{min} and y_{max}, the f_{ios} values are 1.1% and 0.4%, respectively. This minor occurrence of the infeasible overhanging surfaces is primarily attributed to the surface smoothing applied during the post-processing of the discrete elements, particularly in the smooth transition regions.

Figure 12 explains the occurrence of the small infeasible overhanging surfaces after smoothing post-processing through two examples. Discrete element designs often result in numerous sharp angles. Smoothing post-processing is conducted using NURBS (Non-Uniform Rational Basis Spline) surfaces or fillets to mitigate sharp angles and ensure smooth transitions. This treatment conflicts with

Fig. 12 Examples of infeasible overhanging surfaces after smoothing treatment: **a** Smooth transition from $+45°$ to $-45°$ surfaces; **b** Smooth transition along the sharp edges of the frustum of a pyramid

the discrete geometric self-supporting method, leading to small areas that fail to meet the 45° overhang constraints, as highlighted in red in Fig. 12. Consequently, smoothing post-processing inevitably introduces minor overhanging areas. A viable approach to minimizing overhanging areas during smoothing is to increase the number of discrete elements in the topology optimization. From both manufacturing and design perspectives, minor overhanging areas are acceptable. Studies have demonstrated that due to the rheology of the extruded material, features with small infeasible overhanging surfaces can still be printed effectively during the AM process (Calignano 2014; Kranz et al. 2015). The printability of small overhanging surfaces within the formwork is experimentally validated in Sect. 3.4. Furthermore, in some special cases, smooth transitions help avoid stress concentration and improve the mechanical performance of the structure.

In summary, theoretical analysis indicates that utilizing z_{min} as the baseplate for cantilever beam optimization and formwork generation represents the most advantageous choice among the four evaluated printing directions. This strategy ensures that the formwork achieves 100% overhang-free surfaces and the compliance value of the optimized structure is the best.

3.2 3D Messerschmitt–Bölkow–Blohm beam

The second numerical test is a Messerschmitt–Bölkow–Blohm (MBB) beam, whose dimensions and boundary conditions are illustrated in Fig. 13. The design domain is discretized by 8-node cubic elements with a resolution of $160 \times 24 \times 48$. A total uniform load of 100N is applied to the central region of the $y = y_{max}$ plane of the beam. The volume fraction of the design domain is set to 50%.

Figure 14a demonstrates the topology-optimized MBB beam along with the corresponding formwork design using the conventional topology optimization method. Considering the optimized structures exhibiting orthogonal symmetry,
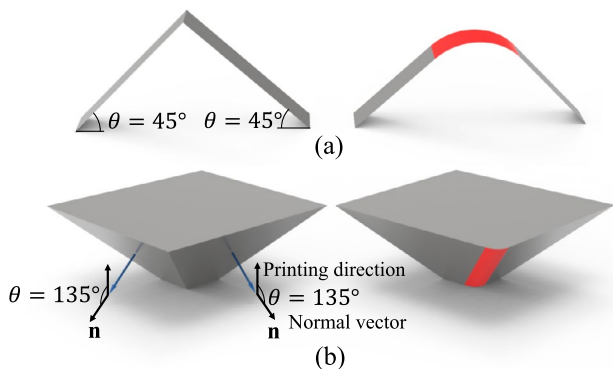
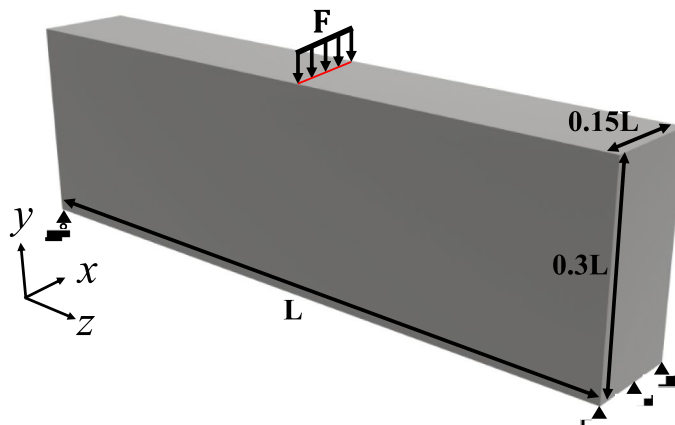**Fig. 13** Design domain and boundary conditions for MBB beam problem in compliance minimization design

Fig. 14 Topology-optimized MBB beams (left) and corresponding formwork (right) by conventional and five-field density approach
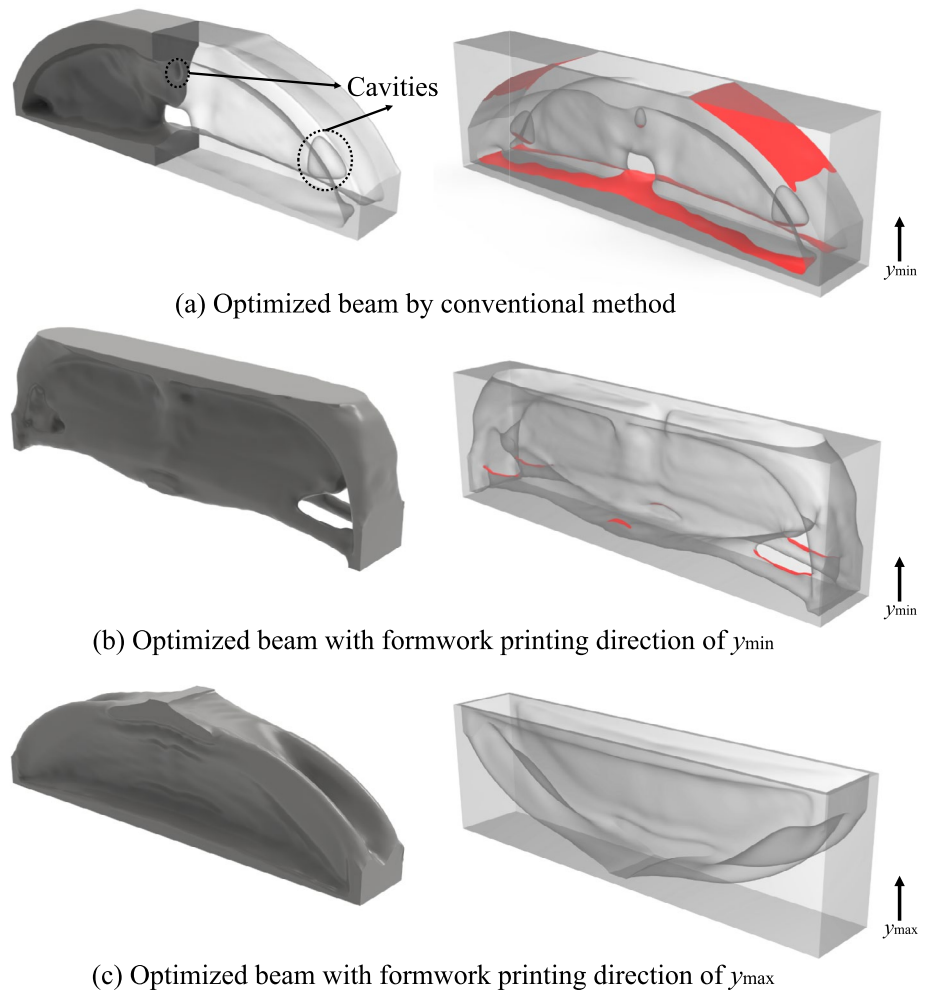

(a) Optimized beam by conventional method

(b) Optimized beam with formwork printing direction of y_{min}

(c) Optimized beam with formwork printing direction of y_{max}

Table 2 A comparison analysis of MBB beam results

Printing baseplate	f_{ios} (Formwork)	f_c (Beam)	Compliance (Beam)	Normalized compliance
Benchmark	17.2%	0.6%	58.45	100%
y_{min}	0.8%	0%	83.20	142.3%
y_{max}	0%	0%	72.73	124.4%

two distinct printing directions are selected for the optimization process. Figure 14b and c presents the optimization results for MBB beams and formwork oriented along the y_{min} and y_{max} printing directions, respectively. A numerical comparative summary is provided in Table 2. Notably, the conventional optimization result (i.e., benchmark design) exhibits the best mechanical performance, evidenced by a compliance value of 58.45. Nonetheless, the corresponding formwork demonstrates significant issues, including severe overhang and internal cavities problems. Specifically, it exhibits an infeasible overhanging surface fraction of $f_{ios} = 17.2\%$ and an internal enclosed cavities fraction of

0.6% within the entire design domain. Following the application of the five-field density approach during the optimization iterations, the internal enclosed cavities fraction can be reduced to $f_c = 0\%$ in both cases, and the infeasible overhanging features have minimized to $f_{ios} = 0.8\%$ and $f_{ios} = 0\%$ for printing baseplate of y_{min} and y_{max}, respectively. Compared to the benchmark result, the compliance values of these two structures increased to 142.3% and 124.4%. This observation is analogous to the previous example involving the cantilever beam, where the optimized structures sacrifice mechanical performance to meet manufacturing constraints.

Under the given loading conditions, the upper section of the MBB beam is designated as the compression zone, while the lower section is identified as the tension zone. A comparison of the optimization results for y_{min} (Fig. 14b) and y_{max} (Fig. 14c) reveals that the most significant difference is in the material distribution. In the y_{min} case, the material is predominantly allocated to the compression zone, leading to a reduced material presence in the tension zone. Conversely, in the y_{max} case, more material is allocated to the tension zone. This discrepancy is the primary factor contributing

to the compliance differences observed between the two structures. It can be concluded that allocating more material to the tension zone yields superior performance.

3.3 3D slab

The third numerical example is a slab design, with the design domain and boundary conditions illustrated in Fig. 15. The dark gray region with a thickness of L/8 is set as a non-optimization domain, whereas the light gray area with dimensions of $4L \times 4L \times L$ is set as the optimization domain. The optimization domain is discretized using a discretization of $96 \times 96 \times 24$ cubic elements. A total uniform load of 1kN is distributed on the $y = y_{max}$ plane of the slab. The $y = y_{min}$ plane incorporates nine square regions ($L/2 \times L/2$) subject to fixed boundary conditions, wherein all displacements are suppressed. The slab problem is optimized with a total volume fraction of 40%.

Figure 16a illustrates the slab structure optimized using the conventional method, which results in a compliance value of 80.00. For a clearer representation of the internal structure, the left side displays a solid representation, while the right side presents a transparent view. It is evident that numerous small internal enclosed cavities are present, which cannot be fabricated using casting. As summarized in Table 3, the volume fraction of these cavities constitutes $f_c = 1.8\%$ of the entire optimization domain. The corresponding original casting formwork exhibits unprintable overhang features on the lower surfaces of these cavities. Despite the infeasible overhanging surface fraction being only $f_{ios} = 0.6\%$, these structures are entirely unmanufacturable without support material since they are in a suspended state within the original formwork.

Figure 16b presents the optimization result for the slab by applying the five-field density approach and setting the printing baseplate to y_{min}. Although the normalized compliance value of the slab structure has increased to 127.5% compared

Fig. 15 Design domain and boundary conditions for slab problem in compliance minimization design
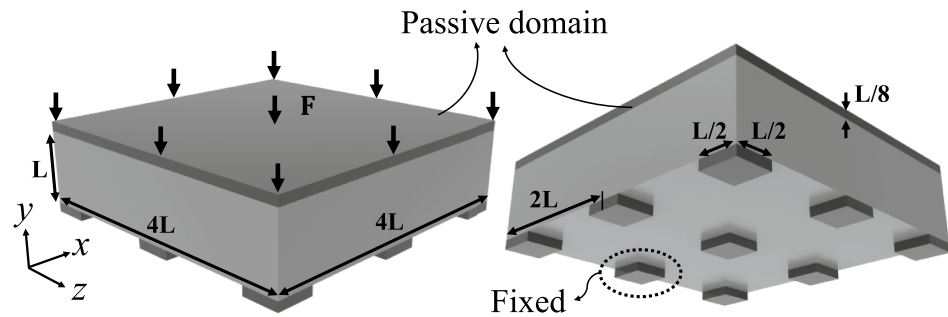

Fig. 16 Bottom view (left) and top view (middle) of topology-optimized slabs and corresponding formwork (right) by conventional and five-field density approach
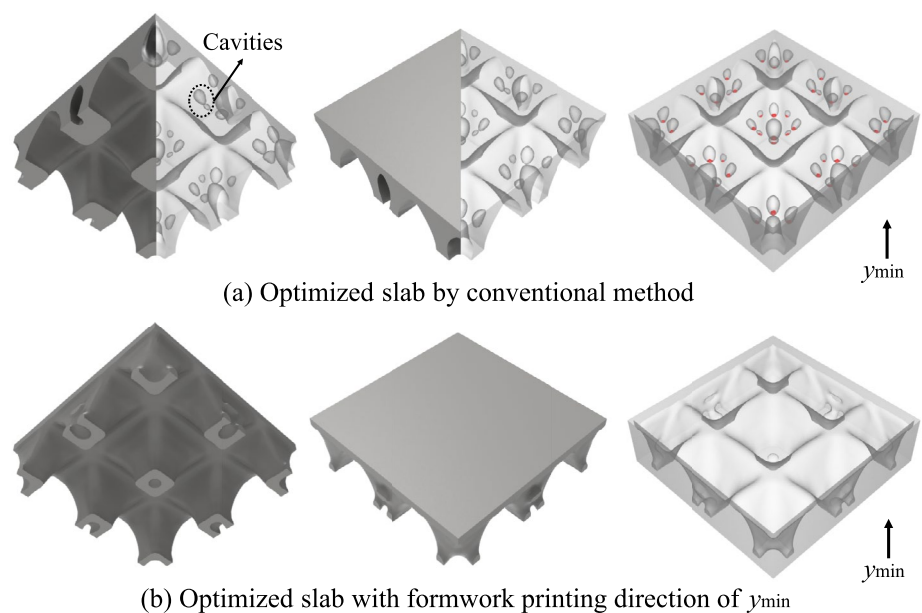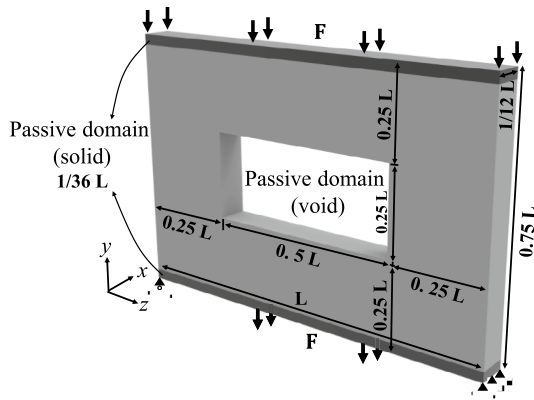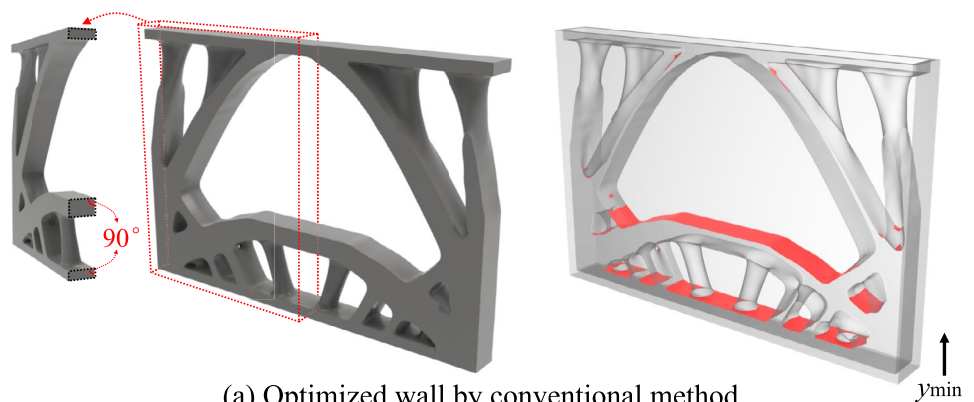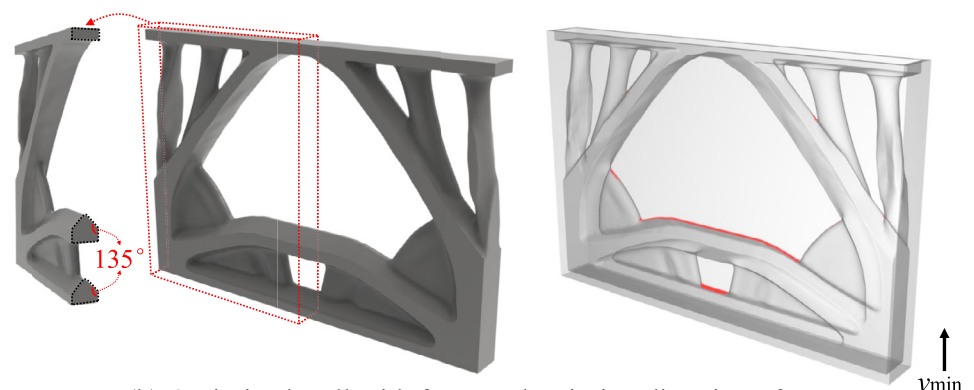

(a) Optimized slab by conventional method

(b) Optimized slab with formwork printing direction of y_{min}

Table 3 A comparison analysis of slab design results

Printing baseplate	f_{ios} (Formwork)	f_c (Slab)	Compliance (Slab)	Normalized compliance
Benchmark	0.6%	1.8%	80.00	100%
y_{min}	0%	0%	101.97	127.5%

Fig. 17 Design domain and boundary conditions for wall problem in compliance minimization design

to the benchmark design, the structure effectively eliminates the occurrence of internal enclosed cavities ($f_c = 0\%$) and infeasible overhanging surfaces ($f_{ios} = 0\%$). This will significantly enhance the manufacturability and application value of the structure.

3.4 3D wall

In the fourth example, a 3D wall problem with passive void and solid domain is considered, as shown in Fig. 17. The entire design domain is discretized into cubic elements with a resolution of $144 \times 12 \times 96$. All displacements at the bottom edges of $z = z_{max}$ and $z = z_{min}$ are suppressed, and a total uniform load of 100N is applied on the top ($y = y_{max}$) and bottom ($y = y_{min}$) plane, respectively. A volume fraction of 40% is pre-defined in the optimization.

Figure 18 shows the walls and formwork optimized by the conventional method and five-field density approach, respectively. Table. 4 presents the data for quantitative comparison. Results demonstrate that both optimized walls do not contain any internal enclosed cavities (i.e., $f_c = 0\%$). The compliance of the benchmark design is 89.76, its corresponding formwork exhibits distinct infeasible overhanging surfaces, with a percentage of $f_{ios} = 9.0\%$. The compliance of the wall optimized using the proposed approach is 92.12, representing a slight increase of 2.6% compared to the benchmark

Fig. 18 Topology-optimized walls (left) and corresponding formwork (right) by conventional and five-field density approach

(a) Optimized wall by conventional method

(b) Optimized wall with formwork printing direction of y_{min}

Table 4 A comparison analysis of wall design results

Printing baseplate	f_{ios} (Formwork)	f_c (Wall)	Compliance (Wall)	Normalized compliance
Benchmark	9.0%	0%	89.76	100%
y_{min}	0.8%	0%	92.12	102.6%

structure. However, the percentage of infeasible overhanging surfaces is reduced to 0.8%, which difference can be obviously observed through the comparison in the right image of Fig. 18. The underlying reason for this difference can be explained from a geometrical perspective. By comparing the cross section of the wall (left image of Fig. 18), the wall optimized using the proposed method forms an inclined plane with an inclined angle of 135°, whereas the benchmark wall has a flat cross-section surface with an angle of 90°. Consequently, this results in different overhang angles in the corresponding formwork.

4 Extension to diverse overhang angles

Different AM technologies impose distinct requirements on overhang angles due to variations in their process characteristics and material behaviors. In this section, an extension of the variable overhang angles is provided by altering the aspect ratio (i.e., $l_x \times l_y \times l_z$) of the finite elements (Fig. 19a). It should be mentioned that the implementation of arbitrary overhang angle constraints presents some challenges, particularly when incompatible with the element's standard aspect ratio or the overall dimensions of the design domain. This incompatibility frequently results in the inability to achieve integer-based element divisions within the design domain, as shown in Fig. 19b. Another challenge arises when α approaches a very small value, causing the elements to become slender, and more elements are required to discretize the domain, which would increase computational costs.

In this example, the same MBB beam configuration as described in Sect. 3.2 is selected. The finite elements with $\alpha = 30°$ are applied to discretize the design domain. A conservative estimation method is employed by rounding down

to the nearest integer for discretization, therefore, the design domain is discretized with a resolution of $160 \times 24 \times 82$.

Figure 20 illustrates the MBB beams and their corresponding formwork obtained under a 30° overhang constraint, with the printing baseplate pre-defined at y_{min} and y_{max}, respectively. Although the topological shapes of the two beams are relatively similar, an analysis of their cross sections reveals that different settings of printing baseplate affect the surface inclination angles. The bottom is accompanied by an inclined feature at an angle of 120° for the case of the printing baseplate of y_{min}, and at an angle of 90° for the case of the printing baseplate of y_{max}. Therefore, it helps in reducing unsupported overhangs during fabrication. Compared to the benchmark structure (Fig. 14a), the compliance of the MBB beams under the 30° overhang constraint increased by only 3.1% and 2.0%, respectively. Furthermore, all infeasible overhanging surfaces and internal enclosed cavities are completely eliminated (i.e., $f_{ios} = 0\%$ and $f_c = 0\%$) (Table 5).
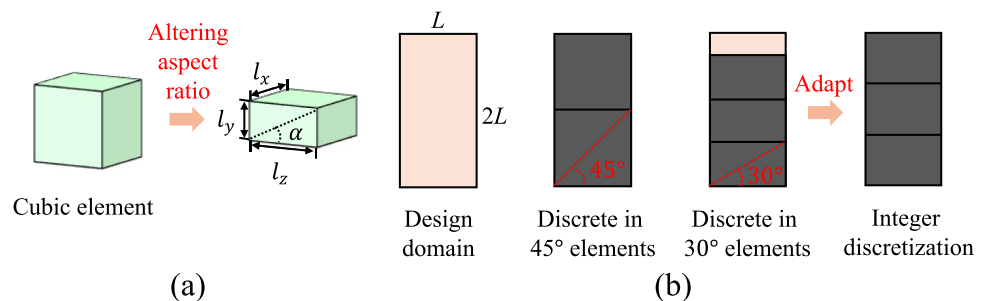
5 Experimental tests

5.1 3D printing experimental tests

In this section, the optimized structures are manufactured using 3D printed formwork and casting techniques to verify the application of the proposed method. It is essential to emphasize that the numerically optimized formwork is designed with a solid cubic outer contour (Fig. 21a). To facilitate demolding and saving printing material and time, the ultra-thin formwork is employed and combined with tree-like supports on the outer surfaces (Fig. 21b). Four optimized cantilever beams in Sect. 3.1 have been chosen as representative examples to demonstrate the effectiveness of formwork printing and the final casting results. The dimensions of the manufactured beams are specified as $150 \times 75 \times 75$ mm.

Details of 3D printing parameters by FFF are provided in Table 6. The thickness of the formwork is set as 0.6 mm to save printing time and facilitate the demolding process. Given that the formwork is intended for casting applications

Fig. 19 **a** Illustration of changing overhang angle by altering aspect ratio; **b** Potential issues and solutions in design domain discretization
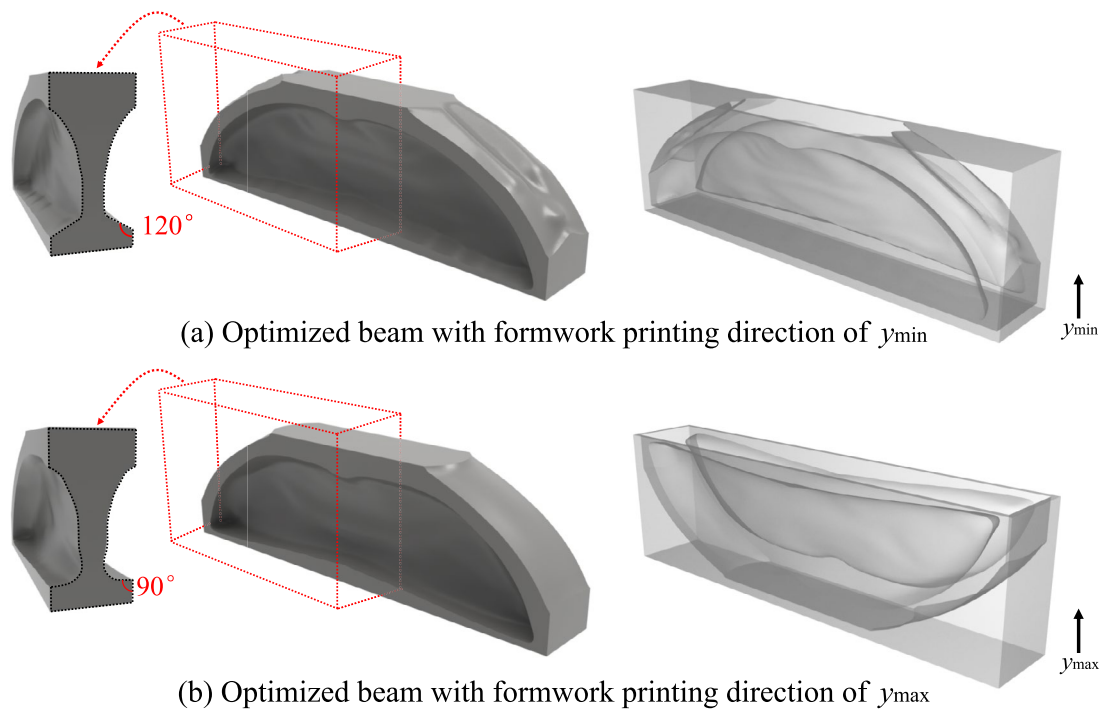

Cubic element

(a)

Design domain   Discrete in 45° elements   Discrete in 30° elements   Integer discretization

(b)

(a) Optimized beam with formwork printing direction of y_{min}

(b) Optimized beam with formwork printing direction of y_{max}

Fig. 20 Illustration of topology-optimized MBB beams, cross sections, and corresponding formwork under a constraint overhang angle of 30°

Table 5 Summarization of MBB beam results under 30° constraint

Printing baseplate	f_{ios} (Formwork)	f_c (Beam)	Compliance (Beam)	Normalized compliance
y_{min}	0%	0%	60.24	103.1%
y_{max}	0%	0%	59.61	102.0%

and has an ultra-thin thickness, non-water-soluble Polylactic acid (PLA) material has been selected for this purpose.

To visually illustrate the benefits of tree-like supports, a quantitative analysis comparing print time and material consumption across the four sets of formwork has been conducted and is summarized in Table 7. According to suggestions from the 3D printing community (Lio 2024),

a 10%-15% infill ratio is commonly used for most prints to support outer surfaces and overcome overhang issues. In this case, the control groups take a 10% grid fill for comparative analysis. Under the above-mentioned printing parameter settings, employing tree-like supports rather than a 10% grid infill can result in time savings ranging from 0.3% to 52.8% and material reductions between 48.3% and 64.2%. The most

Table 6 Parameters for 3D printing by FFF

Printing equipment	Bambu Lab A1 mini
Slicing software	Bambu Studio
Material	PLA, 1.23 g/cm^3
Ultra-thin formwork thickness	0.6mm

Fig. 21 Illustration of 3D formwork printing: **a** Cubic formwork with grid infill type; **b** Ultra-thin formwork with tree-like supports
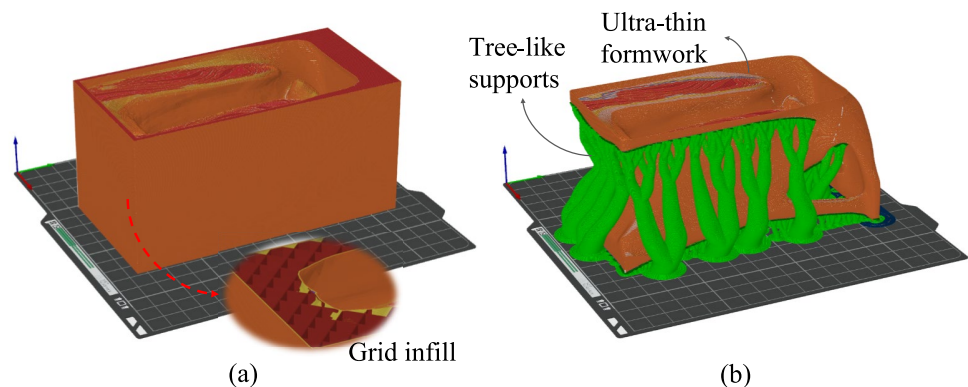
Table 7 A comparative analysis of printing time and material consumption for cantilever beam formwork across various printing directions

Printing baseplate	Printing Time (min)			PLA Material (g)		
	Grid infill	Tree-like supports	Time-saving	Grid infill	Tree-like supports	Material-saving
y_{min}	330	317	3.9%	157.51	81.44	48.3%
y_{max}	295	294	0.3%	146.78	73.15	50.2%
z_{min}	300	177	41.0%	186.18	80.85	56.6%
z_{max}	324	153	52.8%	168.69	60.46	64.2%

optimal time and material savings are achieved when utilizing z_{max} as the baseplate, yielding a 52.8% reduction in printing time and a 64.2% reduction in material consumption, while the total printing time and material consumption are also the lowest of 153 min and 60.46 g, respectively.

Furthermore, Table 7 indicates that the ultra-thin formwork is notably cost-effective. The extension of the present framework to directly design the ultra-thin formwork should be feasible. Directly designing ultra-thin formwork requires that both the internal and external surfaces be free of supports. This implies that, beyond the present framework, a more complex density field filtering process must be developed, or an additional constraint must be introduced to eliminate external surface supports. Therefore, the computational complexity may increase to some extent. To extend the framework to directly design the ultra-thin formwork, some potential challenges related to parameter tuning, algorithmic efficiency, and robustness need to be addressed in further research. This work does not include the extension of this part.

Figure 22 presents a comparison of the internal details of formwork printed using FFF before and after

optimization. The formwork is fabricated with a cubic structure featuring a grid infill, with the profile outline and grid infill delineated in black. Figure 22a illustrates the printing result for the original formwork, which exhibits extensive infeasible overhanging surfaces, necessitating a substantial quantity of internal support material for 3D printing. Figure 22b shows the formwork optimized via the five-field density approach, demonstrating that no internal support material is needed during the printing process. Furthermore, it can be observed that surfaces with minor overhangs remain printable without the need for support. This evidence demonstrates that despite the theoretical formwork presence of small overhanging surfaces, 100% unsupported printing is feasible, attributable to the inherent advantages of the 3D printing process.

Figure 23 illustrates the ultra-thin formwork manufactured via FFF with tree-like supports and the cast beam structures. The application of the five-field density method, in conjunction with the AM formwork filter, facilitated the creation of unsupported features within the formwork, thereby ensuring that all beam structures could

Fig. 22 Illustration of the internal details of printing results: **a** The original formwork for the cantilever beam, with internal support material marked in red; **b** The optimized cantilever beam formwork without internal support material. The profile outline and grid infill for the cubic formwork are marked in black
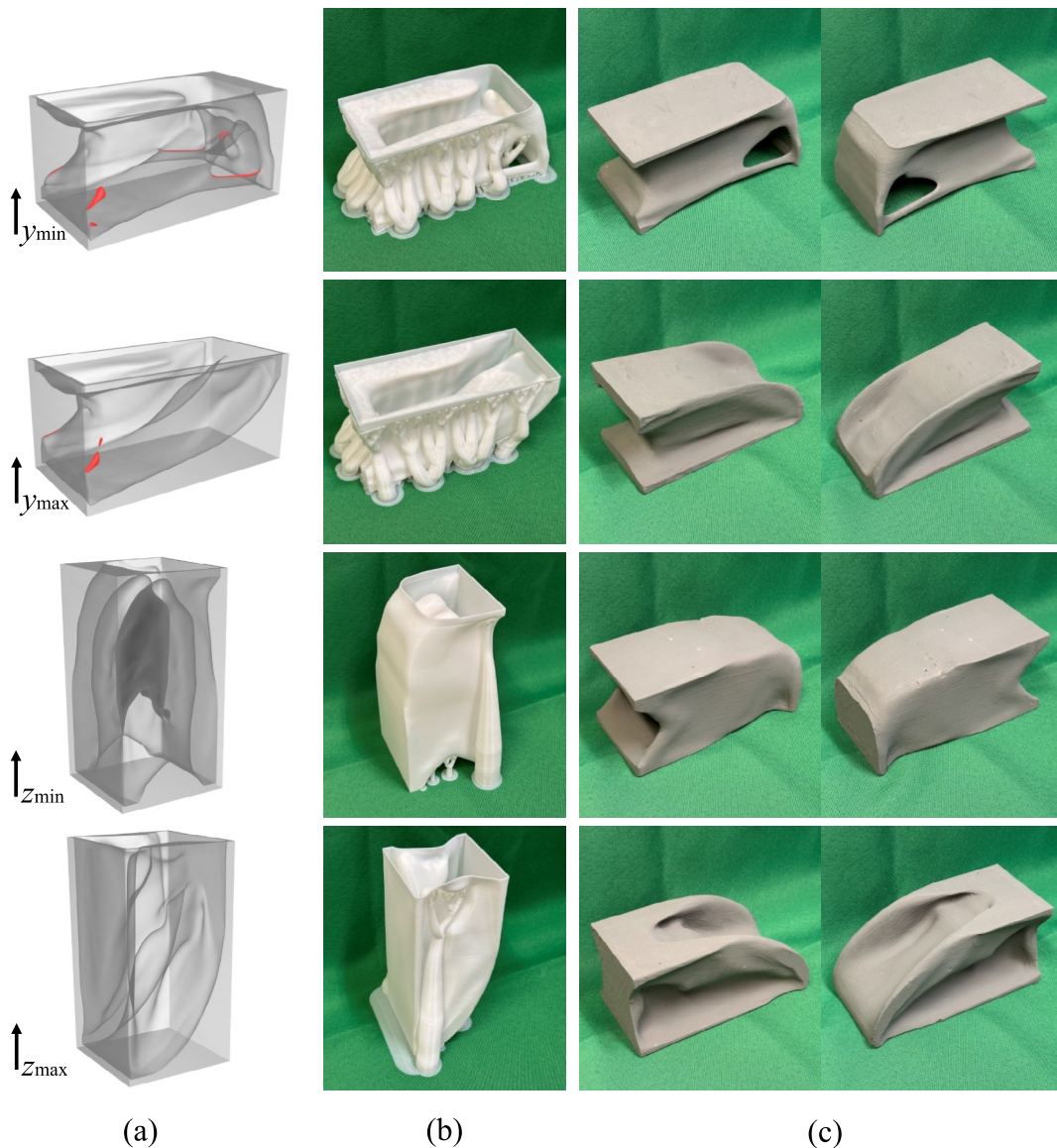

(a)

(b)
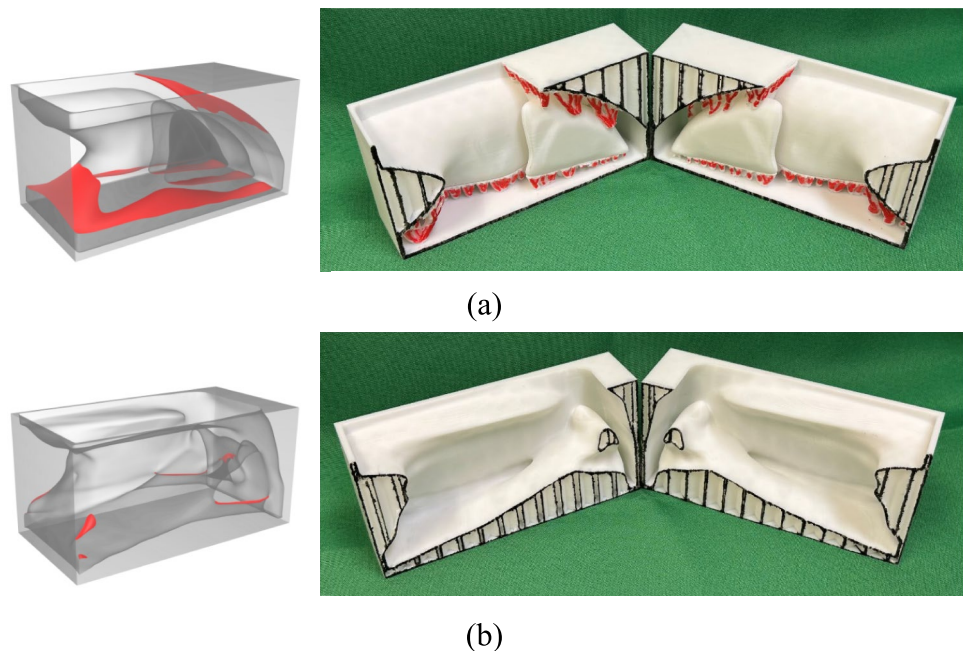
Fig. 23 a Theoretical casting formwork of cantilever beams for various printing directions; **b** 3D printed ultra-thin formwork with tree-like supports; **c** Cantilever beams after demolding

be cast successfully. This further underscores the application of the proposed method.

5.2 Strength tests

This section presents a quantitative strength test to validate the mechanical behavior of the optimized structures. Two typical optimized MBB beams are selected for three-point bending experiments, including 30° and 45° overhang constraints with the printing baseplate of y_{max} (shown in Fig. 14c) and Fig. 20b). The dimensions of the cast MBB beams are specified as $300 \times 45 \times 90$ mm. To ensure the structure maintains good tensile strength and crack resistance, a strain-hardening cementitious composites (SHCC)

material with fiber reinforcement (Teng et al. 2024) is used. Material composition contains ordinary Portland cement (OPC), fly ash (FA), silica fume (SF), quartz sand, polyethylene (PE) fiber, water, high-range water reducer (HRWR), and viscosity modifying agent (VMA), the proportions are listed in Table 8.

The cast specimens (Fig. 25a) were demolded after 24 h and cured for 7 days in an environment with a temperature of 23 °C and relative humidity of 65%. Figure 24 demonstrates the setup for three-point bending tests. The Testometric X500-50 machine was used with a constant loading rate value of 0.5mm/min. The failure mode of the cast specimens is illustrated in Fig. 25b, primarily characterized by the propagation of multiple cracks. This failure mode is

Table 8 Mixture proportions of SHCC (Unit: kg/m³)

OPC	FA	SF	Sand	PE fiber	Water	HRWR	VMA
609	561	79	381	15	390	2.5	0.91
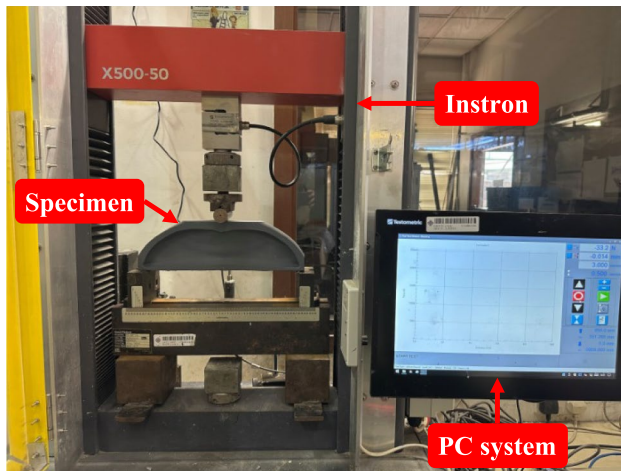
Fig. 24 Experimental setup for three-point bending tests

attributed to the addition of fibers to the material, which enhanced its ductility. The distribution of fibers within the cracks is clearly observed in Fig. 25c.

Figure 26 presents the load–displacement curves, which exhibit a linear increase in the initial phase (i.e., displacement ≤ 0.5 mm). After the displacement exceeds 0.5 mm, a fluctuating upward trend is observed due to the occurrence of cracking and strain-hardening behavior. The ultimate loads of specimens 1 and 2 are 8.27 and 7.14 kN, respectively. Generally, before reaching the ultimate load, specimen 1 exhibits smaller deformation than specimen 2 under the same loading conditions. This is consistent with the numerical results of topology optimization.

According to the numerical results in Tables 2 and 5, the compliance of the beam with a 45° overhang constraint is 22% higher than that of the beam with a 30° overhang constraint. Since compliance is directly related to strain energy, a quantitative comparison of the structure's strain energy can be made by integrating the displacement–load curve. In this case, two integration intervals of 0–2.55 and 0–3.28 mm (i.e., corresponding to points A and C under the same load of 7.14 kN in Fig. 26) are selected as examples for the strain energy calculation. The strain energy values are shown in the bottom right corner of the figure, where it can be observed that the strain energy of specimen 2 is 28% higher than specimen 1. It should be noted that it is assumed that the material is linearly elastic in the topology optimization process, whereas the strain energy calculated in the experiments includes both elastic and plastic phases, which may introduce some errors. In conclusion, the quantitative comparison demonstrates a correlation between the numerical results and the experimental findings, confirming the mechanical effectiveness of the generated topological structures.

6 Conclusion

This study introduces a topology optimization method for designing structures to be cast in AM-produced formwork. An AM formwork filter is built and a five-field density optimization flow is proposed to address the connectivity issue of topology-optimized structures and enable support-free printing of AM-produced formwork. By addressing the self-supporting issue of the formwork, the floating parts in
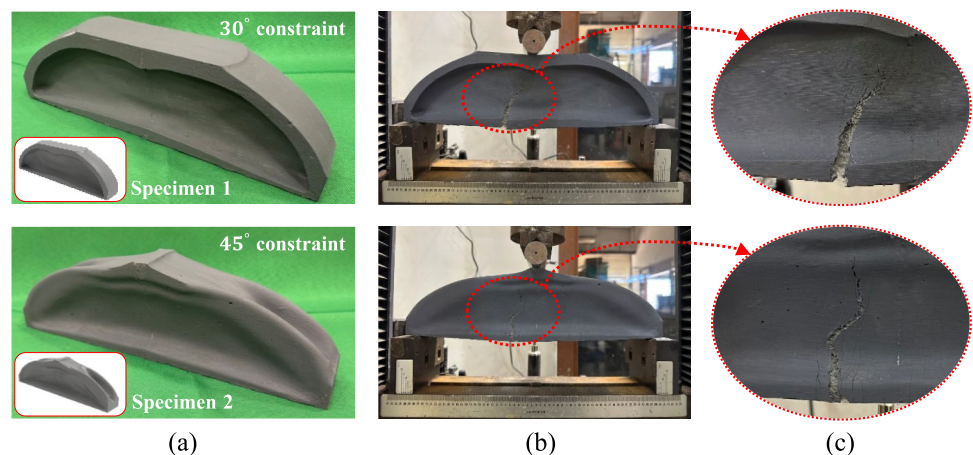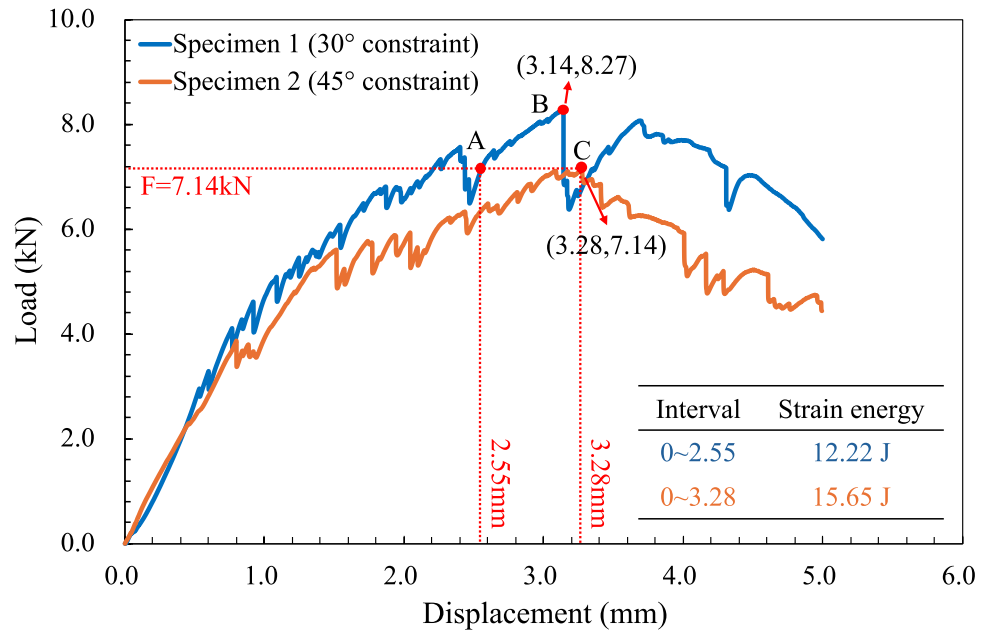
Fig. 25 **a** Cast specimens of MBB beam; **b** Failure mode under three-point bending tests; **c** Main cracks and the fibers embedded within the cracks

(a)   (b)   (c)

Fig. 26 Load–displacement curves for three-point bending tests

the optimized structures are avoided, and thus connectivity issue of the optimized structures is solved. This optimization framework ensures that the topology-optimized structures are devoid of internal enclosed cavities and that the corresponding formwork can be produced via 3D printing without the need for internal support material. Additionally, the method allows for customization of the printing direction, enabling diverse topological structures and formwork.

The effectiveness, stability, and extensibility of the proposed method have been validated through several typical numerical 3D examples. Although the compliance value of the structures increased relative to the benchmark results, the structures optimized using the proposed method completely eliminate internal enclosed cavities and reduce infeasible overhanging surfaces by over 98.9%. Furthermore, this study experimentally demonstrates that minor infeasible overhanging surfaces generated during the smoothing process can be fully printed without the need for support material. In practical formwork manufacturing, ultra-thin formwork is recommended to conserve printing materials and reduce printing time. The three-point bending strength tests are also provided to demonstrate the mechanical behavior of the optimized structures.

The proposed method is anticipated to further bridge the gap between topology optimization, AM, and practical construction procedures. Future developments may extend this method by incorporating various 3D printing parameters, printer performance, and processes to accommodate a broader range of printing scenarios. Moreover, since it has been observed that additional manufacturing constraints may negatively impact structural performance, it is essential to explore feasible strategies to balance manufacturability

and mechanical performance. This study has verified that the structural performance varies with customized printing directions. Therefore, it is suggested that future work considers the printing direction as an optimization variable to enable the simultaneous optimization of topology and the printing orientation.

Appendix A. Sensitivity analysis

When applying the five-field density approach, the sensitivities with respect to the initial density vector $\boldsymbol{\rho}$ can be determined by the chain rule, which is as follows:

$$\frac{\partial \varphi}{\partial \boldsymbol{\rho}} = \frac{\partial \mathbf{x}}{\partial \boldsymbol{\rho}} \frac{\partial \mathbf{x}_f}{\partial \mathbf{x}} \frac{\partial \mathbf{x}_{AM}}{\partial \mathbf{x}_f} \frac{\partial \mathbf{x}_c}{\partial \mathbf{x}_{AM}} \frac{\partial \varphi}{\partial \mathbf{x}_c} \tag{A.1}$$

where φ represents objective function c or material volume V in the compliance minimization problem. The sensitivities associated with the function are detailed in the following paragraphs.

(1)   The sensitivities of the compliance function c and material volume V with respect to the castable density $x_{c,e}$ are expressed as follows:

$$\frac{\partial c}{\partial x_{c,e}} = -\mathbf{U}^T \frac{\partial \mathbf{K}}{\partial x_{c,e}} \mathbf{U} = -p\left(x_{c,e}\right)^{p-1}\left(E_0 - E_{\min}\right)\mathbf{u}_{c,e}^T \mathbf{k}_0 \mathbf{u}_{c,e}, \ \left(x_{c,e} \in \mathbf{x}_c\right) \tag{A.2}$$

$$\frac{\partial V}{\partial x_{c,e}} = 1, \ \left(x_{c,e} \in \mathbf{x}_c\right) \tag{A.3}$$

where $\mathbf{u}_{c,e}$ is the displacement vector of element e.

(2) The sensitivity of the castable density vector $\mathbf{x}_c$ with respect to the filtered formwork density vector $\mathbf{x}_{AM}$ is given by

$$\frac{\partial \mathbf{x}_c}{\partial \mathbf{x}_{AM}} = \mathrm{diag}(-\mathbf{1}) \tag{A.4}$$

where *diag*() denotes the transformation of a vector into a diagonal matrix.

(3) The sensitivities of objective and constraint functions with respect to $\mathbf{x}_f$ by chain rule are expressed as follows:

$$\frac{\partial \varphi}{\partial \mathbf{x}_f} = \frac{\partial \mathbf{x}_{AM}}{\partial \mathbf{x}_f} \frac{\partial \varphi}{\partial \mathbf{x}_{AM}} \tag{A.5}$$

where the sensitivity of $\partial \varphi / \partial \mathbf{x}_{AM}$ can be determined in terms of Eqs. (A.2, A.3, and A.4), which is as follows:

$$\frac{\partial \varphi}{\partial \mathbf{x}_{AM}} = \frac{\partial \mathbf{x}_c}{\partial \mathbf{x}_{AM}} \frac{\partial \varphi}{\partial \mathbf{x}_c} \tag{A.6}$$

The sensitivity of the filtered formwork density $\mathbf{x}_{AM}$ with respect to the initial formwork density $\mathbf{x}_f$ needs to be determined. However, based on the principle proposed in Sect. 2.3, since the density $\mathbf{x}_{AM}$ in layer j depends on the density of the underlying layers (i.e., layer $j-1$), the computational cost and memory requirements are significantly higher than anticipated. Therefore, the adjoint method is employed to compute the sensitivity. Here, the filtered formwork density $\mathbf{x}_{AM}$ corresponds to the actual printed density $\mathbf{p}$ in Eq. (7), i.e., $\mathbf{x}_{AM} = \mathbf{p}$. For conciseness, $\mathbf{p}$ will be used in place of $\mathbf{x}_{AM}$ in the subsequent derivation. The sensitivity is given by

$$\frac{\partial \varphi}{\partial \mathbf{x}_{f,j}} = \frac{\partial \mathbf{p}_j}{\partial \mathbf{x}_{f,j}} \boldsymbol{\lambda}_j \tag{A.7}$$

where j represents the layer index ($1 \le j \le n_y$, with n_y representing the total number of layers), $\boldsymbol{\lambda}_j$ denotes the Lagrangian multipliers for layer j, which is defined as follows:

$$\begin{cases} \boldsymbol{\lambda}_j = \dfrac{\partial \varphi}{\partial \mathbf{p}_j} + \dfrac{\partial \mathbf{p}_{j+1}}{\partial \mathbf{p}_j} \boldsymbol{\lambda}_{j+1}, (1 \le j < n_y) \\ \boldsymbol{\lambda}_{n_y} = \dfrac{\partial \varphi}{\partial \mathbf{p}_{n_y}}, (j = n_y) \end{cases} \tag{A.8}$$

Refer to Eqs. (7 and 8), the terms $\partial \mathbf{p}_j / \partial \mathbf{x}_{f,j}$ and $\partial \mathbf{p}_{j+1} / \partial \mathbf{p}_j$ are derived as follows:

$$\frac{\partial \mathbf{p}_j}{\partial \mathbf{x}_{f,j}} = \mathrm{diag}\left[\frac{1}{2}\left(1 - (\mathbf{x}_{f,j} - \mathbf{p}_{a,j}) \circ \left((\mathbf{x}_{f,j} - \mathbf{p}_{a,j})^{\circ 2} + \varepsilon \right)^{\circ -1/2} \right) \right] \tag{A.9}$$

$$\frac{\partial \mathbf{p}_{j+1}}{\partial \mathbf{p}_j} = \frac{\partial \mathbf{p}_{a,j+1}}{\partial \mathbf{p}_j} \frac{\partial \mathbf{p}_{j+1}}{\partial \mathbf{p}_{a,j+1}} \tag{A.10}$$

where

$$\frac{\partial p_{j+1}}{\partial p_{a,j+1}} = \frac{1}{2}\left(1 + (x_{f,j} - p_{a,j})\left((x_{f,j} - p_{a,j})^2 + \varepsilon \right)^{-1/2} \right) \tag{A.11}$$

$$\frac{\partial p_{a,j+1}(p_{j,1}, \ldots, p_{j,n})}{\partial p_{j,e'}} = \frac{\exp(\alpha p_{j,e'})}{\sum\limits_{e=1}^{n} \exp(\alpha p_{j,e})} [1 + \alpha(p_{j,e'} - p_{a,j+1})] \tag{A.12}$$

By substituting Eqs. (A.8) and (A.9) into Eq. (A.7), the sensitivities of the objective and constraint functions with respect to initial formwork density $\mathbf{x}_f$ can be determined on a layer-by-layer basis. A detailed derivation is provided in Appendix B.

(4) The sensitivity of the initial formwork density $\mathbf{x}_f$ with respect to the structural density $\mathbf{x}$ has the following form:

$$\frac{\partial \mathbf{x}_f}{\partial \mathbf{x}} = \mathrm{diag}(-\mathbf{1}) \tag{A.13}$$

(5) The sensitivity of the structural density $\mathbf{x}$ with respect to the initial design density $\boldsymbol{\rho}$ is derived as follows:

$$\frac{\partial \mathbf{x}}{\partial \boldsymbol{\rho}} = \mathbf{H}_s^T \tag{A.14}$$

Appendix B. Sensitivity of AM formwork filter by adjoint method

Equations (7 and 8) indicate that the actual printed density in layer l ($\mathbf{p}_l$) is a function in terms of $\mathbf{x}$ and $\mathbf{p}_{l-1}$. Therefore, it can be written as follows:

$$\mathbf{p}_l = \mathbf{f}(\mathbf{x}_l, \mathbf{p}_{l-1}) = \mathbf{f}_l \tag{B.1}$$

By using the adjoint method, the function can be expressed as follows:

$$\varphi = \hat{\varphi} = \varphi(\mathbf{p}) + \sum_{l=1}^{n_y} \boldsymbol{\lambda}_l^T (\mathbf{f}_l - \mathbf{p}_l) \tag{B.2}$$

Differentiation of Eq. (B.2) gives the following:

$$\frac{\partial \varphi}{\partial \mathbf{x}_j} = \frac{\partial \hat{\varphi}}{\partial \mathbf{x}_j} = \sum_{l=1}^{n_y} \left[\frac{\partial \mathbf{p}_l}{\partial \mathbf{x}_j} \frac{\partial \varphi}{\partial \mathbf{p}_l} + \left(\delta_{lj}\mathbf{I}\frac{\partial \mathbf{f}_l}{\partial \mathbf{x}_l} + \frac{\partial \mathbf{p}_{l-1}}{\partial \mathbf{x}_j} \frac{\partial \mathbf{f}_l}{\partial \mathbf{p}_{l-1}} - \frac{\partial \mathbf{p}_l}{\partial \mathbf{x}_j} \right) \boldsymbol{\lambda}_l \right] \tag{B.3}$$

where δ_{lj} is the Kronecker delta ($l=j$, $\delta_{lj}=1$; $l \neq j$, $\delta_{lj}=0$), l and j are the layer indexes. For $j > l$, $\partial \mathbf{p}_l / \partial \mathbf{x}_j = \mathbf{0}$ due to printed densities only depending on the initial density in underlying layers. Equation (B.3) can be written as follows:

$$\frac{\partial \varphi}{\partial \mathbf{x}_j} = \frac{\partial \mathbf{p}_j}{\partial \mathbf{x}_j} \frac{\partial \varphi}{\partial \mathbf{p}_j} + \sum_{l=j+1}^{n_y} \left[\frac{\partial \mathbf{p}_l}{\partial \mathbf{x}_j} \left(\frac{\partial \varphi}{\partial \mathbf{p}_l} - \lambda_l \right) + \frac{\partial \mathbf{p}_{l-1}}{\partial \mathbf{x}_j} \frac{\partial \mathbf{f}_l}{\partial \mathbf{p}_{l-1}} \lambda_l \right] \tag{B.4}$$

Equation (B.4) can be expanded as follows:

$$\frac{\partial \varphi}{\partial \mathbf{x}_j} = \frac{\partial \mathbf{p}_j}{\partial \mathbf{x}_j} \frac{\partial \varphi}{\partial \mathbf{p}_j} + \sum_{l=j+1}^{n_y} \frac{\partial \mathbf{p}_l}{\partial \mathbf{x}_j} \left(\frac{\partial \varphi}{\partial \mathbf{p}_l} - \lambda_l \right)$$
$$+ \frac{\partial \mathbf{p}_j}{\partial \mathbf{x}_j} \frac{\partial \mathbf{f}_{j+1}}{\partial \mathbf{p}_j} \lambda_{j+1} + \sum_{l=j+2}^{n_y} \frac{\partial \mathbf{p}_{l-1}}{\partial \mathbf{x}_j} \frac{\partial \mathbf{f}_l}{\partial \mathbf{p}_{l-1}} \lambda_l \tag{B.5}$$

The last term is the summation from $l=j+2$ to $l=n_y$, it can be changed into a summation from $l=j+1$ to $l=n_y$-1 by reindexing, which is as follows:

$$\sum_{l=j+2}^{n_y} \frac{\partial \mathbf{p}_{l-1}}{\partial \mathbf{x}_j} \frac{\partial \mathbf{f}_l}{\partial \mathbf{p}_{l-1}} \lambda_l = \sum_{l=j+1}^{n_y-1} \frac{\partial \mathbf{p}_l}{\partial \mathbf{x}_j} \frac{\partial \mathbf{f}_{l+1}}{\partial \mathbf{p}_l} \lambda_{l+1} \tag{B.6}$$

Similarly, the first summations can be expanded as follows:

$$\sum_{l=j+1}^{n_y} \frac{\partial \mathbf{p}_l}{\partial \mathbf{x}_j} \left(\frac{\partial \varphi}{\partial \mathbf{p}_l} - \lambda_l \right) = \frac{\partial \mathbf{p}_{n_y}}{\partial \mathbf{x}_j} \left(\frac{\partial \varphi}{\partial \mathbf{p}_{n_y}} - \lambda_{n_y} \right) + \sum_{l=j+1}^{n_y-1} \frac{\partial \mathbf{p}_l}{\partial \mathbf{x}_j} \left(\frac{\partial \varphi}{\partial \mathbf{p}_l} - \lambda_l \right) \tag{B.7}$$

Substituting Eqs. (B.6 and B.7) into Eq. (B.5), it has

$$\frac{\partial \varphi}{\partial \mathbf{x}_j} = \frac{\partial \mathbf{p}_j}{\partial \mathbf{x}_j} \left(\frac{\partial \varphi}{\partial \mathbf{p}_j} + \frac{\partial \mathbf{f}_{j+1}}{\partial \mathbf{p}_j} \lambda_{j+1} \right) + \frac{\partial \mathbf{p}_{n_y}}{\partial \mathbf{x}_j} \left(\frac{\partial \varphi}{\partial \mathbf{p}_{n_y}} - \lambda_{n_y} \right)$$
$$+ \sum_{l=j+1}^{n_y-1} \frac{\partial \mathbf{p}_l}{\partial \mathbf{x}_j} \left(\frac{\partial \varphi}{\partial \mathbf{p}_l} - \lambda_l + \frac{\partial \mathbf{f}_{l+1}}{\partial \mathbf{p}_l} \lambda_{l+1} \right) \tag{B.8}$$

Since the Lagrange multipliers can be chosen arbitrarily, and as mentioned in Eq. (B.1), $\mathbf{p} = \mathbf{f}$, the chosen multipliers satisfy the following conditions:

$$\begin{cases} \lambda_l = \dfrac{\partial \varphi}{\partial \mathbf{p}_l} + \dfrac{\partial \mathbf{p}_{l+1}}{\partial \mathbf{p}_l} \lambda_{l+1}, (1 \leq l < n_y) \\ \lambda_{n_y} = \dfrac{\partial \varphi}{\partial \mathbf{p}_{n_y}}, (l = n_y) \end{cases} \tag{B.9}$$

Therefore, Eq. (B.8) can be simplified as follows:

$$\frac{\partial \varphi}{\partial \mathbf{x}_j} = \frac{\partial \mathbf{p}_j}{\partial \mathbf{x}_j} \left(\frac{\partial \varphi}{\partial \mathbf{p}_j} + \frac{\partial \mathbf{p}_{j+1}}{\partial \mathbf{p}_j} \lambda_{j+1} \right) = \frac{\partial \mathbf{p}_j}{\partial \mathbf{x}_j} \lambda_j \tag{B.10}$$

Declarations

References

Abdulhameed O, Al-Ahmari A, Ameen W, Mian SH (2019) Additive manufacturing: challenges, trends, and applications. Adv Mech Eng 11(2):1687814018822880. https://doi.org/10.1177/1687814018822880

Allaire G, Jouve F, Toader A-M (2002) A level set method for shape optimization. CR Math 334:1125–1130. https://doi.org/10.1016/S1631-073X(02)02412-3

Andreassen E, Clausen A, Schevenels M, Lazarov BS, Sigmund O (2011) Efficient topology optimization in MATLAB using 88 lines of code. Struct Multidisc Optim 43:1–16. https://doi.org/10.1007/s00158-010-0594-7

Bendsoe MP, Sigmund O (2013) Topology optimization: theory, methods, and applications. Springer, Singapore

Bi M, Tran P, Xie YM (2020) Topology optimization of 3D continuum structures under geometric self-supporting constraint. Addit Manuf 36:101422. https://doi.org/10.1016/j.addma.2020.101422

Bos F, Wolfs R, Ahmed Z, Salet T (2016) Additive manufacturing of concrete in construction: potentials and challenges of 3D concrete printing. Virt Phys Prototyp 11(3):209–225. https://doi.org/10.1080/17452759.2016.1209867

Brackett D, Ashcroft I, Hague R (2011) Topology optimization for additive manufacturing. In: 2011 International solid freeform fabrication symposium. https://doi.org/10.26153/tsw/15300

Burger J, Lloret-Fritschi E, Scotto F, Demoulin T, Gebhard L, Mata-Falcón J, Gramazio F, Kohler M, Flatt RJ (2020) Eggshell: ultrathin three-dimensional printed formwork for concrete structures. 3D Print Addit Manuf 7(2):48–59. https://doi.org/10.1089/3dp.2019.0197

Calignano F (2014) Design optimization of supports for overhanging structures in aluminum and titanium alloys by selective laser melting. Mater des 64:203–213. https://doi.org/10.1016/j.matdes.2014.07.043

Gaynor AT, Meisel NA, Williams CB, Guest JK (2014) Topology optimization for additive manufacturing: considering maximum overhang constraint. In: 15th AIAA/ISSMO multidisciplinary analysis and optimization conference. p 2036. https://doi.org/10.2514/6.2014-2036

Gibson I, Rosen DW, Stucker B, Khorasani M, Rosen D, Stucker B, Khorasani M (2021) Additive manufacturing technologies. Springer, Cham, p 17

Guo X, Zhang W, Zhong W (2014) Doing topology optimization explicitly and geometrically—a new moving morphable components based framework. J Appl Mech 81(8):081009. https://doi.org/10.1115/1.4027609

Guo X, Zhou J, Zhang W, Du Z, Liu C, Liu Y (2017) Self-supporting structure design in additive manufacturing through explicit topology optimization. Comput Methods Appl Mech Eng 323:27–63. https://doi.org/10.1016/j.cma.2017.05.003

Huang X, Xie YM (2007) Convergent and mesh-independent solutions for the bi-directional evolutionary structural optimization method. Finite Elem Anal des 43(14):1039–1049. https://doi.org/10.1016/j.finel.2007.06.006

Huang X, Xie YM (2010) Evolutionary topology optimization of continuum structures: methods and applications. Wiley, Chichester

Jipa A, Dillenburger B (2022) 3D printed formwork for concrete: State-of-the-art, opportunities, challenges, and applications. 3D Print Addit Manuf 9(2):84–107. https://doi.org/10.1089/3dp.2021.0024

Jipa A, Bernhard M, Dillenburger B (2020) Submillimeter formwork: 3D-printed plastic formwork for concrete elements. In: 2017 TxA emerging design+ technology conference proceedings. pp 70–79. https://doi.org/10.3929/ethz-b-000237359

Kranz J, Herzog D, Emmelmann C (2015) Design guidelines for laser additive manufacturing of lightweight structures in TiAl6V4. J Laser Appl. https://doi.org/10.2351/1.4885235

Kristiawan RB, Imaduddin F, Ariawan D, Ubaidillah Arifin Z (2021) A review on the fused deposition modeling (FDM) 3D printing: filament processing, materials, and printing parameters. Open Eng 11(1):639–649. https://doi.org/10.1515/eng-2021-0063

Langelaar M (2016) Topology optimization of 3D self-supporting structures for additive manufacturing. Addit Manuf 12:60–70. https://doi.org/10.1016/j.addma.2016.06.010

Langelaar M (2017) An additive manufacturing filter for topology optimization of print-ready designs. Struct Multidisc Optim 55:871–883. https://doi.org/10.1007/s00158-016-1522-2

Leschok M, Dillenburger B (2019) Dissolvable 3DP formwork. In: Ubiquity and autonomy—proceedings of the ACADIA conference. pp 188–196.

Li S, Yuan S, Zhu J, Wang C, Li J, Zhang W (2020) Additive manufacturing-driven design optimization: Building direction and structural topology. Addit Manuf 36:101406. https://doi.org/10.1016/j.addma.2020.101406

Li S, Yuan S, Zhu J, Zhang W, Tang Y, Wang C, Li J (2022) Optimal and adaptive lattice design considering process-induced material anisotropy and geometric inaccuracy for additive manufacturing. Struct Multidisc Optim 65(1):35. https://doi.org/10.1007/s00158-021-03153-1

Lio MD (2024) 3D printing infill: patterns & densities for stronger prints

Ma G, Li Z, Wang L, Wang F, Sanjayan J (2019) Mechanical anisotropy of aligned fiber reinforced composite for extrusion-based 3D printing. Constr Build Mater 202:770–783. https://doi.org/10.1016/j.conbuildmat.2019.01.008

Mertens R, Clijsters S, Kempen K, Kruth J-P (2014) Optimization of scan strategies in selective laser melting of aluminum parts with downfacing areas. J Manuf Sci Eng 136(6):061012. https://doi.org/10.1115/1.4028620

Najmon JC, Raeisi S, Tovar A (2019) Review of additive manufacturing technologies and applications in the aerospace industry. Addit Manuf Aerosp Ind. https://doi.org/10.1016/B978-0-12-814062-8.00002-9

Qian X (2017) Undercut and overhang angle control in topology optimization: a density gradient based integral approach. Int J Numer Meth Eng 111(3):247–272. https://doi.org/10.1002/nme.5461

Sethian JA, Wiegmann A (2000) Structural boundary design via level set and immersed interface methods. J Comput Phys 163(2):489–528. https://doi.org/10.1006/jcph.2000.6581

Sigmund O (2001) A 99 line topology optimization code written in Matlab. Struct Multidisc Optim 21(2):120–127. https://doi.org/10.1007/s001580050176

Sigmund O (2007) Morphology-based black and white filters for topology optimization. Struct Multidisc Optim 33:401–424. https://doi.org/10.1007/s00158-006-0087-x

Sigmund O, Maute K (2013) Topology optimization approaches: a comparative review. Struct Multidisc Optim 48(6):1031–1055. https://doi.org/10.1007/s00158-013-0978-6

Singh S, Ramakrishna S (2017) Biomedical applications of additive manufacturing: present and future. Curr Opin Biomed Eng 2:105–115. https://doi.org/10.1016/j.cobme.2017.05.006

Teng F, Ye J, Yu J, Li H, Weng Y, Mechtcherine V (2024) Development of strain-hardening cementitious composites (SHCC) as bonding materials to enhance interlayer and flexural performance of 3D printed concrete. Cement Concr Compos 152:105657

Wang MY, Wang X, Guo D (2003) A level set method for structural topology optimization. Comput Methods Appl Mech Eng 192:227–246. https://doi.org/10.1016/S0045-7825(02)00559-5

Wang D, Yang Y, Yi Z, Su X (2013) Research on the fabricating quality optimization of the overhanging surface in SLM process. Int J Adv Manuf Technol 65:1471–1484. https://doi.org/10.1007/s00170-012-4271-4

Weng Y, Li M, Ruan S, Wong TN, Tan MJ, Yeong KLO, Qian S (2020) Comparative economic, environmental and productivity assessment of a concrete bathroom unit fabricated through 3D printing and a precast approach. J Clean Prod 261:121245. https://doi.org/10.1016/j.jclepro.2020.121245

Wong KV, Hernandez A (2012) A review of additive manufacturing. International scholarly research notices 2012. https://doi.org/10.5402/2012/208760

Xie YM, Steven GP (1992) Shape and layout optimization via an evolutionary procedure. In: Proceedings of the international conference on computational engineering science.

Xie YM, Steven GP (1993) A simple evolutionary procedure for structural optimization. Comput Struct 49(5):885–896. https://doi.org/10.1016/0045-7949(93)90035-C

Xiong Y, Yao S, Zhao Z-L, Xie YM (2020) A new approach to eliminating enclosed voids in topology optimization for additive manufacturing. Addit Manuf 32:101006. https://doi.org/10.1016/j.addma.2019.101006

Zhang W, Yuan J, Zhang J, Guo X (2016) A new topology optimization approach based on moving morphable components (MMC) and the ersatz material model. Struct Multidisc Optim 53:1243–1260. https://doi.org/10.1007/s00158-015-1372-3

Zhang W, Chen J, Zhu X, Zhou J, Xue D, Lei X, Guo X (2017) Explicit three dimensional topology optimization via moving

morphable void (MMV) approach. Comput Methods Appl Mech Eng 322:590–614. https://doi.org/10.1016/j.cma.2017.05.002

Zhang W, Li D, Zhou J, Du Z, Li B, Guo X (2018) A moving morphable void (MMV)-based explicit approach for topology optimization considering stress constraints. Comput Methods Appl Mech Eng 334:381–413. https://doi.org/10.1016/j.cma.2018.01.050

Zhao Z-L, Zhou S, Cai K, Xie YM (2020) A direct approach to controlling the topology in structural optimization. Comput Struct 227:106141. https://doi.org/10.1016/j.compstruc.2019.106141

Zhou L, Zhang W (2019) Topology optimization method with elimination of enclosed voids. Struct Multidisc Optim 60:117–136. https://doi.org/10.1007/s00158-019-02204-y